140 (2022) 213042

Contents lists available at ScienceDirect

Biomaterials Advances

journal homepage: www.journals.elsevier.com/materials-science-and-engineering-c

Interplay of surface polarization charge, dynamic electrical stimulation and compositional modification towards accelerated osteogenic response of $Na_xK_{1-x}NbO_3$ piezo-bioceramics

Deepak Khare, Priya Singh, Ashutosh Kumar Dubey *

Department of Ceramic Engineering, Indian Institute of Technology (BHU), Varanasi 221005, INDIA

ARTICLE INFO

Keywords:
Surface polarization charge
Dynamic pulsed electrical stimulation
Sodium potassium niobate
Piezo-bioceramics
Osteogenic response

ABSTRACT

Bone remodeling processes involve endogenous bioelectrical signals such as piezoelectric charges. Moreover, external electrical stimulation helps in improving the healing capability of injured tissues by modulating the metabolic signaling pathways of cells. Towards this end, the present study reveals the influence of the combined action of electrostatic surface polarization charge and dynamic pulsed electrical stimulation alongwith compositional modification towards improving the osteogenic response of emerging piezo-bioceramics, sodium potassium niobate [$Na_xK_{1-x}NbO_3$ (x = 0.2–0.8), NKN]. The dependence of crystal structure on compositions (x) was retrieved by Rietveld refinement and X-ray peak profile analyses. The surface charge, stored in the polarized (@ 25 kV at 500 °C) $Na_xK_{1-x}NbO_3$ (x = 0.2, 0.5, 0.8) samples were measured to be 0.52, 0.50 and 0.47 μC/cm^2, respectively, using thermally stimulated depolarized current (TSDC). X-ray photoelectron spectroscopy (XPS) survey scan spectra revealed that the polarization process does not alter the surface chemistry of NKN. Negatively charged surfaces are observed to accelerate early-stage adhesion of osteoblast-like cells which further results in enhanced spreading of adhered cells. Subsequently, the dynamic pulsed electrical stimulation of 1 V/cm with the pulse duration of 400 μs was applied, while the cells were being adhered on electrostatically charged surfaces. The quantitative and qualitative analyses revealed that the synergistic action of electrostatic surface polarization charge and dynamic pulsed electrical stimulation further accelerates cell proliferation and differentiation on negatively charged surfaces of Na and K-rich compositions of NKN. The mechanism of augmented cellular activity was analyzed using intracellular Ca^{2+} measurement.

1. Introduction

Endogenous piezoelectric potential of natural living bone plays a crucial role in various essential structural remodeling processes such as growth, repair and regeneration [1–3]. Similar to the bone, electrical treatment or mechanical loading on the piezoelectric bioceramics develops polarization surface charges which promote bone regeneration by modulating the cellular activities such as adhesion, proliferation, differentiation, etc. [2–5]. Recently, polarization induced improved biocompatibility of piezoelectric bioceramics has been suggested as an appealing approach to develop new-generation electroactive prosthetic orthopedic implants [2,3]. Apart from internal bioelectrical cues, the potentiality of external electrical stimulation has also been revealed in improving the healing capability of damaged tissues such as bone, cartilage and ligaments [6,7,8,9]. The application of direct electrical stimulation helps in regulating cellular metabolism via the activation of metabolic signaling pathways of cells [3,7,8].

Among various piezoelectric bioceramics, sodium potassium niobate has recently been recognized as an emerging prospective candidate for electro-active orthopedic implant applications [3,5,10,11,12,13]. Chen et al. [5] observed about 1.3 times higher protein adsorption on the negatively as well as positively polarized (@ 25 kV) surfaces of $Na_{0.5}K_{0.5}NbO_3$ as compared to its non-polarized counterpart. Yao et al. [14] reported a significant increase in the viability and projected areas of rat bone marrow mesenchymal stem cells, while adhered on the positively polarized (@ 25 kV) surface of $Na_{0.5}K_{0.5}NbO_3$ than those on the non-polarized surface. In recent studies, Verma et al. [15,16] observed augmented proliferation of osteoblast cells on dynamic pulsed electric field treated polarized samples of hydroxyapatite (HA) / 1393 bioglass - $Na_{0.5}K_{0.5}NbO_3$ composites. Interestingly, $Na_xK_{1-x}NbO_3$ (x =

* Corresponding author.
E-mail address: akdubey.cer@iitbhu.ac.in (A.K. Dubey).

https://doi.org/10.1016/j.bioadv.2022.213042
Received 24 May 2022; Received in revised form 10 July 2022; Accepted 19 July 2022
Available online 25 July 2022

0.2–0.8) [NKN] is also observed to be antibacterial in nature which can potentially overcome the issue of prosthetic infection, associated with the existing orthopedic implants [14,15,16,17].

The Na and K ions participate in regulating the metabolism of the human body such as water-mineral balancing, maintaining nerve impulse, muscle contraction-relaxation, regulating blood pressure and cellular homeostasis [18,19]. Recent studies reported the potentiality of Nb for hard tissue regeneration [20,21,22,23,24,25].

Considering above backdrops, the present study explored the combined effect of electrostatic surface charge, dynamic pulsed electrical stimulation and compositional modification towards accelerating osteogenic response of NKN. The hydroxyapatite (HA) was chosen as control because HA resembles mineral component (natural apatite) of living bone and has long been studied as a bone graft material [11,26,27]. The effect of compositional variation in NKN on its structural parameters was analyzed using Rietveld refinement and X-ray peak profile analyses. Further, the mechanical properties were examined. Inductively coupled plasma-atomic emission spectroscopy (ICP-AES) was performed to understand the leaching behavior of NKN in simulated body fluid (SBF). The charges, stored in NKN samples by polarization (@ 25 kV) treatment were quantified using thermally stimulated depolarized current (TSDC) measurement. Further, the effect of polarization on surface chemistry and wettability was examined using X-ray photoelectron spectroscopy (XPS) and contact angle measurement, respectively. The influence of surface charge on early-stage cell adhesion was studied. Thereafter, the synergistic effect of electrostatic surface polarization charge and dynamic electrical stimulation alongwith compositional modification on cell proliferation, adhesion and differentiation were analyzed. To understand the mechanism of electrostatic/dynamic pulsed electrical stimulation induced cellular response through the activation of signaling pathways, the concentrations of intracellular Ca^{2+} were measured for the non-treated and treated samples.

2. Experimental procedure

2.1. Synthesis

The $Na_xK_{1-x}NbO_3$ (x = 0.2–0.8) samples were synthesized using solid-state route [17]. The obtained powder was compacted in circular pellets (diameter: 10 mm, height: 1 mm) with conventional pressing. The fabricated pellets were further cold isostatically pressed with a pressure of 300 MPa, before sintering. The optimized sintering temperature for $Na_{0.2}K_{0.8}NbO_3$, $Na_{0.5}K_{0.5}NbO_3$ and $Na_{0.8}K_{0.2}NbO_3$ samples were 1010, 1075 and 1120 °C for 2 h, respectively. In addition, HA was prepared via coprecipitation route [17,28]. The powder samples of HA were also compacted in circular pellets of similar dimensions as NKN, using conventional pressing, which was further cold isostatically pressed and then sintered at 1200 °C for 2 h.

2.2. Structural investigations

The X-ray diffraction (XRD) patterns, for $Na_xK_{1-x}NbO_3$ (x = 0.2–0.8) ceramics, were recorded from X-ray diffractometer (Rigaku Miniflex II Desktop) with Cu-Kα (wavelength, λ = 1.54 Å) radiation. The data was collected over the diffraction angle range of 20–60° in the step size of 0.02. Rietveld analyses (using the Full Prof Suit program) were performed to retrieve the information on structural changes with compositional variation in NKN. XRD patterns were also analyzed via X-ray peak profile analyses by considering the broadening of intense peaks. The crystallite size and strain were evaluated using Scherrer, modified Scherrer, Williamson-Hall plot, and size-strain plot methods.

2.3. Mechanical properties

The resistance of fabricated NKN and HA pellets against indentation, abrasion or penetration was measured using Vicker's hardness tester (Digi-test, VTP-6046) with an applied load of 5 kgf (dwell period: 10 s). The height and thickness of the circular pellets were kept as 10 mm and 2 mm, respectively, and a diamond indenter of pyramidal shape was used for operation. The experiment was performed according to the standard protocol, using the following formula (Eq. (1)) [ASTM E384], [29]:

$$H_v = 1.854\frac{F}{d^2} \tag{1}$$

where, F and d indicate the applied load (kgf) and average diagonal length, respectively. The mean value of three indentations for each pellet was used for comparison.

The compressive strength of NKN and HA pellets was examined with a universal testing machine (Tinius Olsen). The test was performed according to ASTM C773, specialized for compression tests. The height and diameter of circular pellets were kept to be 15 mm and 10 mm, respectively. The cross-head speed was kept at 0.5 mm/min. The ultimate compressive strength of samples was quantified using the Eq. (2):

$$\sigma_C = \frac{\text{Applied load (N)}}{\text{cross sectional area (mm}^2\text{)}} \tag{2}$$

2.4. Ion leaching

To understand the actual leaching behavior of prepared compositions of NKN in the biological fluid, the ion leaching study was performed. For this purpose, the concentration of leached ions (Na^+ and K^+) from NKN pellets in SBF (pH; 7.4, prepared by Kokubo's method) [30] was measured using ICP-AES (iCAP 6000 Series, Thermofisher Scientific). The sintered pellets of NKN were kept in SBF (10 mg/ml) for 7, 14 and 21 days at 37 °C. The pH of the solution was maintained at 7.4 throughout the experiment. After the specified period of time, the obtained solutions from each sample were diluted 10 times in ultrapure water and then filtered using 0.2 μm sterile filter, before measurements.

2.5. Polarization treatment

For this purpose, the diamond finished sample pellets were exposed to corona at the applied voltage of 25 kV at 500 °C, for 30 min. Thereafter, the samples were cooled under the application of constant voltage (25 kV) upto room temperature. The distance between the surface of the sample and the corona tip was kept to about 1 cm. The surface of the pellet with the direct exposure of corona was negatively polarized (Neg. Pol.) and the opposite surface was positively polarized (Pos. Pol.), as per the manufacturer's guideline.

2.6. Surface charge measurement

To evaluate the charge, stored in the polarized $Na_xK_{1-x}NbO_3$ pellets and to investigate the influence of polarization on the crystal structure, TSDC measurement was performed. For this purpose, the polarized NKN samples were depolarized by heating the pellets from room temperature to 500 °C, with a heating rate of 5 °C/min. During this period, the TSDC spectrum was recorded using a Femto/Picoammeter (B2981A, Keysight).

2.7. X-ray photoelectron spectroscopy (XPS)

XPS analyses were performed to understand the influence of polarization on the surface chemistry of the $Na_xK_{1-x}NbO_3$ sample. The survey spectra for non-polarized (non-Pol.) and polarized samples were scanned using an X-ray photoelectron spectrometer (Thermo Fisher Scientific).

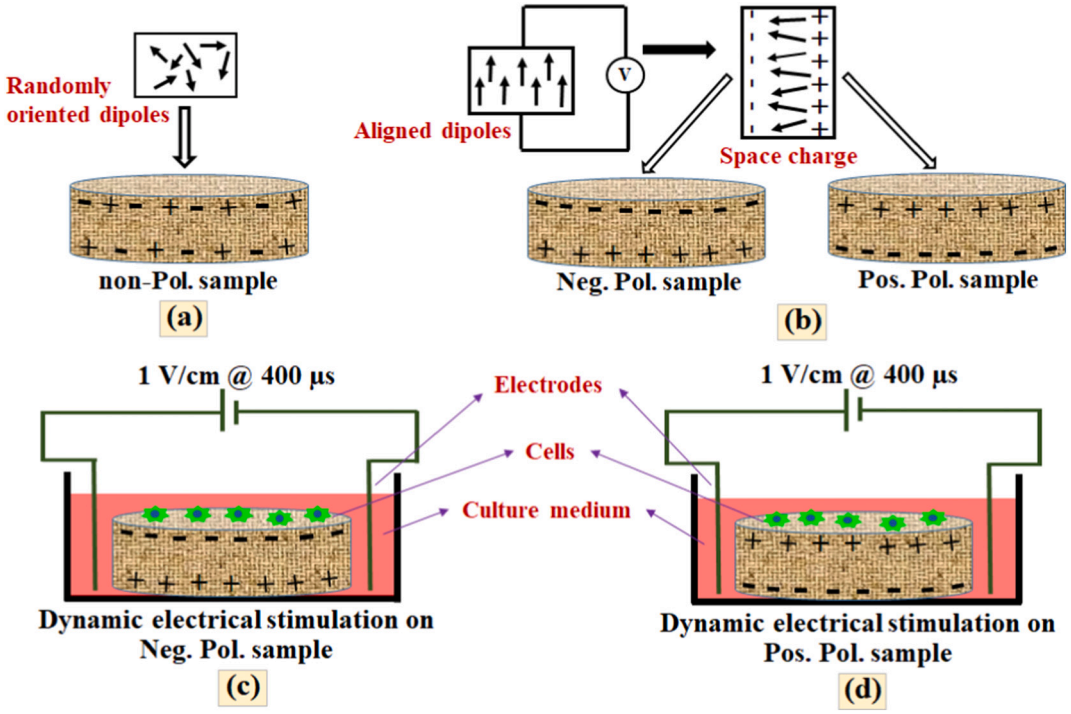

Fig. 1. Schematic representing the application of dynamic electrical stimulation on the cells, adhered on polarized surfaces. (a) The non-Pol. samples with randomly oriented dipoles, (b) Dipoles alignment in the polarized (@ 25 kV) samples and the development of negative and positive surface charges. The application of dynamic electrical stimulation (1 V/cm, 400 µs), while cells are being adhered on the (c) Neg. Pol. (d) Pos. Pol. surfaces.

2.8. Contact angle measurement

The contact angle on the non-Pol. and polarized $Na_xK_{1-x}NbO_3$ and HA control samples were examined with deionized (DI) water and cell growth media to observe the influence of surface charge on the hydrophilicity. For this purpose, a contact angle measurement unit (KRUSS GmbH, DSA10) was used.

2.9. Cellular response

Cell culture experiments have been performed to evaluate the viability of MG-63 and human bone marrow mesenchymal stem cells (hMSCs) on the non-Pol. and polarized $Na_xK_{1-x}NbO_3$ and HA (control). MG-63, the human osteosarcoma cells, was procured from (NCCS Pune, Maharashtra) and hMSCs (HiFi™) were obtained from Himedia labs. The MG-63 cells were cultured at 37 °C (5 % CO_2 and relative humidity: 95 %) in DMEM medium (Dulbecco's modified eagle medium, high glucose powder, Gibco) supplemented with 15 % fetal bovine serum (FBS, Gibco) and antibiotics (1 %, Antibiotic-Antimycotic, Gibco). However, hMSCs were grown in expansion media (HiMesoXL™, Himedia) with a similar supplementary medium and environment. In the confluent layer of cells, a small amount of 0.25 % Trypsin – EDTA (Gibco) solution was added to the culture flask for detaching the cells from the surface. The viable cells were counted using a hemocytometer and Axiovert 25 microscope (Carl Zeiss AG). After counting, 2×10^4 cells/ml were seeded on each sample and then incubated in the respective medium at 37 °C (5 % CO_2 and relative humidity: 95 %). The culture medium was replaced with fresh media after every 48 to 72 h.

2.9.1. Effect of surface polarization on the initial adhesion of cells

Morphology of MG-63 cells, adhered on the non-Pol. and polarized surfaces of $Na_xK_{1-x}NbO_3$ and HA (control samples), were observed after 6 h of cell seeding. The cells, adhered on the samples were fixed using paraformaldehyde (Himedia) and then permeabilized using Triton X-100 (SRL). These permeabilized cells were blocked by the addition of bovine serum albumin (BSA, SRL). Thereafter, the nuclei and cytoskeletons of the adhered cells were stained with DAPI (Invitrogen) and Alexafluor 488 Phalloidin (Invitrogen) dyes, respectively. The imaging of the stained cells was performed using a fluorescence microscope (Nikon Eclipse, LV 100 ND). The projected areas of the randomly selected 20 cells, adhered on the samples were measured for comparison, using Image J software.

2.9.2. Synergistic effect of surface polarization and dynamic electrical stimulation on cellular response

For this purpose, the cells were allowed to adhere on the non-Pol. and polarized $Na_xK_{1-x}NbO_3$ and control samples. Further, a pulsed electric field (1 V/cm for a pulse duration of 400 µs) was applied on the cells after 12 and 24 h of seeding with a digital oscilloscope (SMO702, ScientiFic) [Fig. 1]. The timings for the application of pulsed electric field was chosen depending upon the growth pattern (doubling time) of MG-63 cell line (~24–28 h) [31,32] and human bone marrow mesenchymal stem cells (~26 h) [33].

2.9.2.1. MTT assay. Cell proliferation study was performed using MG-63 and hMSCs cells, after 3, 5 and 7 days of culture on the non-Pol. and polarized $Na_xK_{1-x}NbO_3$ samples as well as control. After the stipulated incubation period, the growth media was removed from each sample. After rinsing with PBS (phosphate buffer saline), the reconstituted MTT (MTT: media ratio kept at 1:10) was added to each sample and again incubated for 6 h, at 37 °C (5 % CO_2 and relative humidity: 95 %) to permit the formation of formazan crystals by reacting live cells with reconstituted MTT. Thereafter, the obtained solution was replaced with dimethyl sulfoxide (DMSO, SRL) for the dissolution of formazan crystals. Further, the concentration of these formazan crystals was measured as optical density using ELISA microplate (iMark Bio-rad) reader, at 595 nm. The outcomes, obtained from the samples, were statistically analyzed using SPSS (IBM) software. The significant differences among the examined samples were analyzed using the ANOVA technique. Tukey and Games-Howell tests, at $p < 0.05$, were used for the

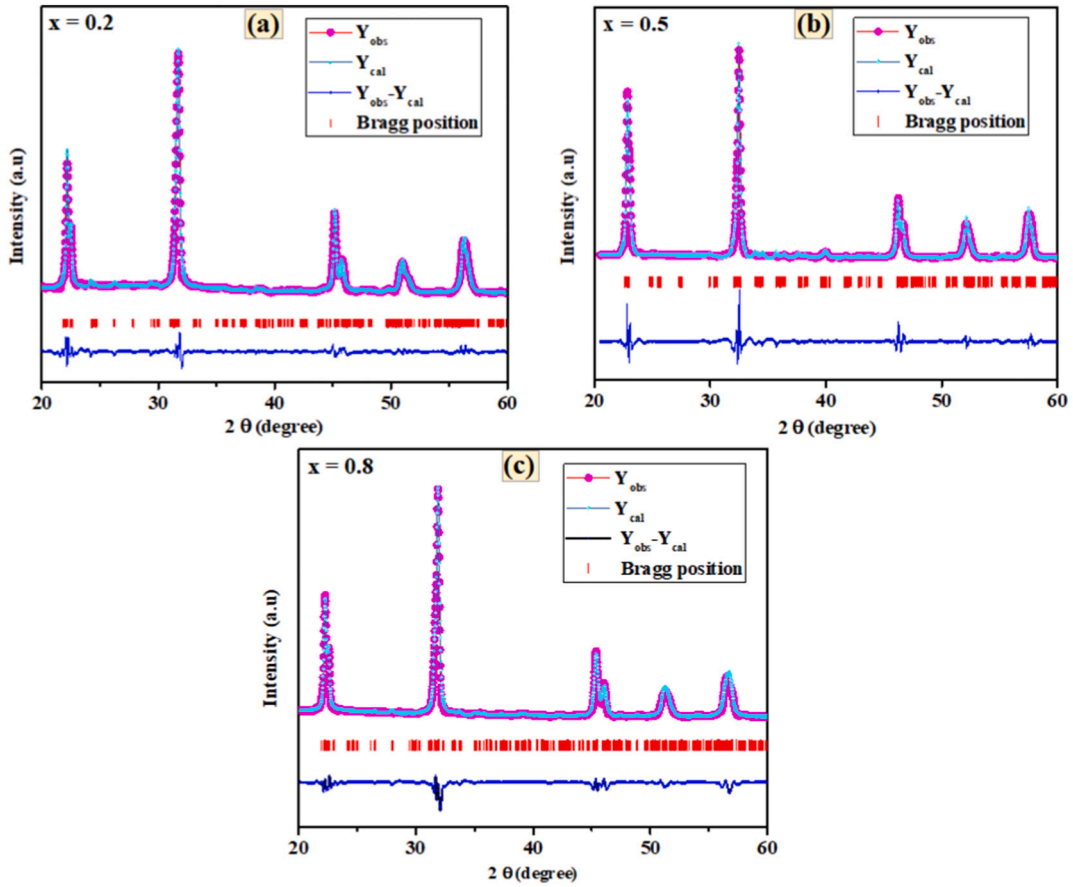

Fig. 2. Rietveld refinement analyses for NKN samples. The plots represent the observed and refined data for sintered $Na_xK_{1-x}NbO_3$, (a) x = 0.2, (b) 0.5 and (c) 0.8.

Table 1
The final obtained values of various refined parameters, corresponding to monoclinic phases in $Na_xK_{1-x}NbO_3$ (x = 0.2, 0.5, 0.8) samples, sintered at 1010, 1075 and 1120 °C, respectively.

	$Na_xK_{1-x}NbO_3$		
	$Na_{0.2}K_{0.8}NbO_3$	$Na_{0.5}K_{0.5}NbO_3$	$Na_{0.8}K_{0.2}NbO_3$
χ^2	1.21	1.09	1.07
R_p	25.8	13.0	16.2
R_{wp}	28.3	14.8	17.4
R_{exp}	25.7	14.1	17
R_f	6.9	7.15	6.5
GOF	1.10	1.05	1.02

Post Hoc multiple comparisons.

2.9.2.2. Alkaline phosphatase (ALP) activity. ALP assay was used for the assessment of the osteogenic potential of the developed scaffolds with MG-63 cells, after 7 and 14 days of incubation. ALP activity is an early biomarker of osteoblast differentiation and therefore, indicates the neo bone-formation ability on the seeded scaffolds [34,35]. Moreover, ALP activity depicts several precise biological processes including the initiation of biomineralization, etc. [35,36]. The osteogenic culture media was prepared by adding 0.2 mM L-ascorbic acid (Sigma) and 10 mM β-Glycerol phosphate (Himedia) in DMEM, supplemented with FBS and antibiotics.

The non-Pol. and polarized $Na_xK_{1-x}NbO_3$ and control samples were seeded with MG-63 cells, at a density of 2×10^4 cells/ml. The seeded samples were incubated in the prepared osteogenic culture media in a CO_2 incubator (5 % CO_2 and relative humidity: 95 %). The electrical stimulation (1 V/cm with a pulse duration of 400 μs) was applied to the wells after 12 and 24 h of incubation to observe the effect of dynamic electrical stimulation on the ALP activity. After stipulated period of time, the seeded cells were lysed using Triton X-100 (50 μl of 0.1 %) for 5 min. Subsequently, 200 μl of *p*-nitrophenyl phosphate (PNP, Himedia) was added to each sample and further incubated for 1 h at 37 °C. After that, the reaction was ceased by the addition of 2 N NaOH (100 μl). Finally, the absorbance of the obtained solution was taken in triplicate at 405 nm using ELISA microplate reader. The ALP activities of the samples were normalized with BSA standard curve.

2.9.2.3. Morphological analyses. The adhesion and morphology of

Table 2
Geometrical parameters of solid state synthesized $Na_xK_{1-x}NbO_3$ (x = 0.2, 0.5, 0.8) samples, sintered at 1010, 1075 and 1120 °C, respectively.

Samples	X-ray peak profile analyses					
	Scherrer Method	Modified Scherrer method	Williamson-Hall plot		Size-strain plot	
	Crystallite size (D) in nm	D (nm)	D (nm)	Lattice Strain (ε)	D (nm)	Lattice Strain (ε)
$Na_{0.2}K_{0.8}NbO_3$	17.98	21.78	27.012	2.3×10^{-3}	16.87	0.2×10^{-3}
$Na_{0.5}K_{0.5}NbO_3$	18.65	26.09	49.76	3.8×10^{-3}	28.45	2.2×10^{-3}
$Na_{0.8}K_{0.2}NbO_3$	17.54	22.12	28.91	2.7×10^{-3}	16.13	–

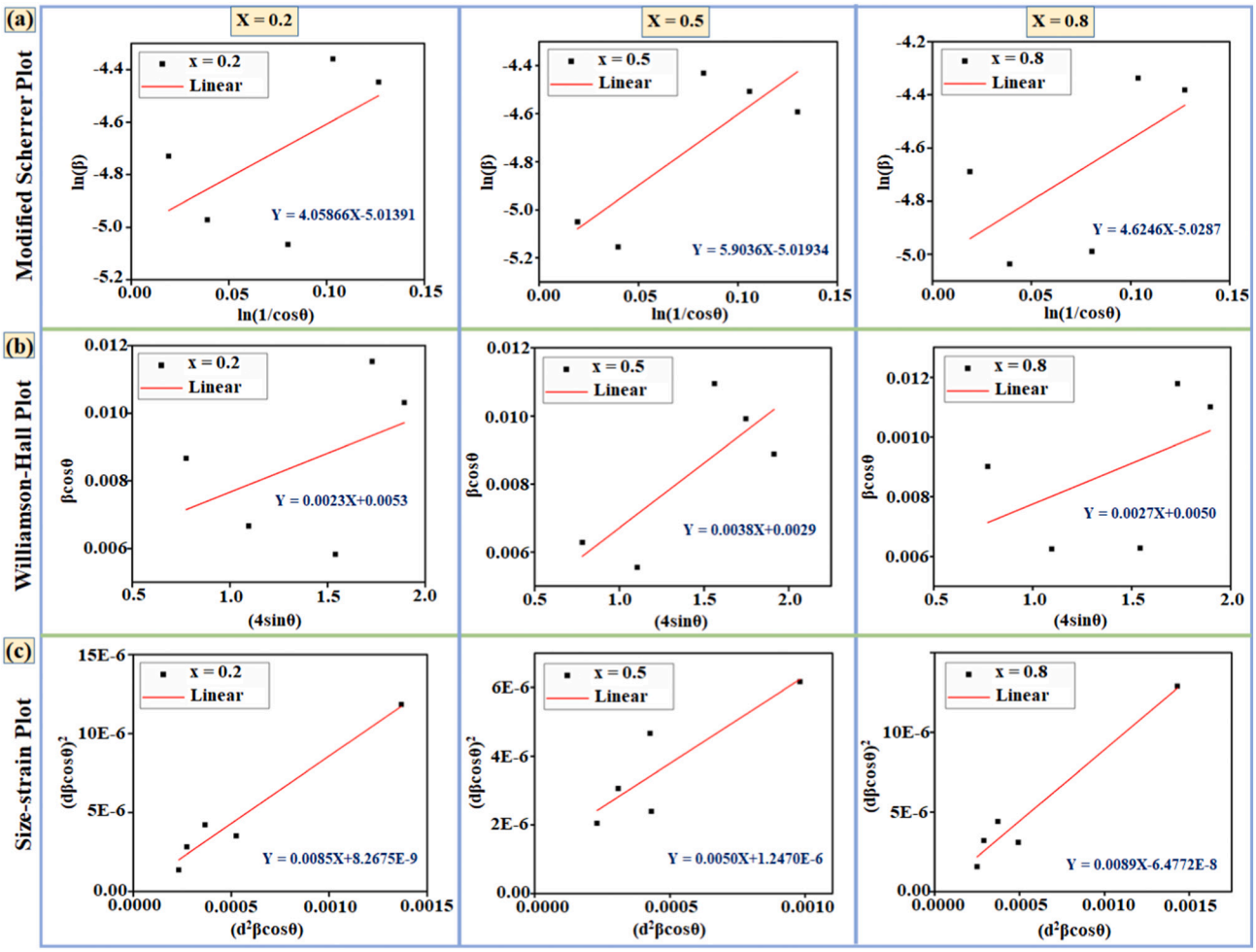

Fig. 3. X-ray peak profile analyses for $Na_xK_{1-x}NbO_3$ (x = 0.2, 0.5, 0.8) samples. Representation of plots, obtained from (a) Modified Scherrer, (b) Williamson-Hall, and (c) Size-strain methods for $Na_xK_{1-x}NbO_3$ samples.

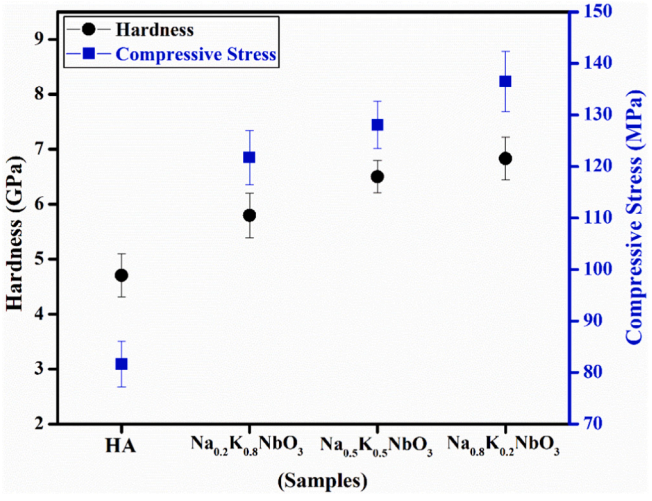

Fig. 4. Mechanical properties of $Na_xK_{1-x}NbO_3$ (x = 0.2, 0.5, 0.8) and HA samples. Hardness and compressive strength of sintered specimens of $Na_xK_{1-x}NbO_3$ and HA.

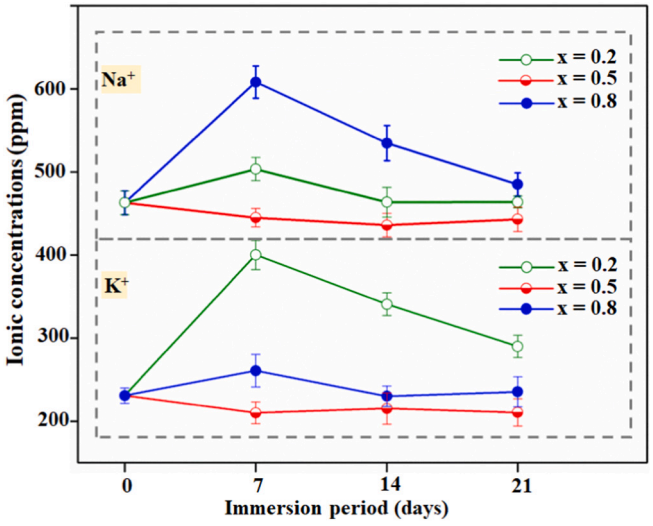

Fig. 5. Na^+ and K^+ leaching profiles from $Na_xK_{1-x}NbO_3$ (x = 0.2, 0.5, 0.8) in SBF. The plot represents the dynamic changes in concentrations of Na^+ and K^+, after immersion of $Na_xK_{1-x}NbO_3$ samples in SBF.

hMSCs cells on $Na_xK_{1-x}NbO_3$ samples and control were observed using fluorescence microscopy. After 3 days of seeding, the cells, adhered on the samples were fixed using paraformaldehyde and then permeabilized with Triton X-100. These permeabilized cells were blocked by the addition of bovine serum albumin (BSA). Thereafter, the nuclei and

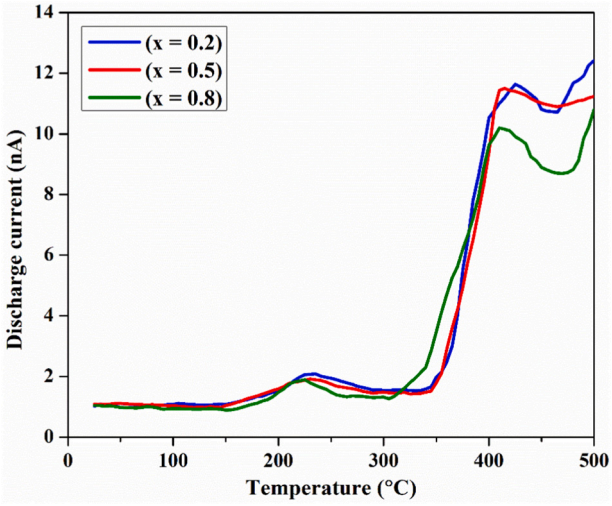

Fig. 6. Thermally stimulated depolarization current (TSDC) measurement. TSDC spectra of for $Na_xK_{1-x}NbO_3$ (x = 0.2, 0.5, 0.8) ceramics, polarized at 25 kV, followed by depolarization at the heating rate of 5 °C/min. upto 500 °C.

cytoskeletons were stained with DAPI and Alexafluor dyes, respectively. The stained cells were observed using a fluorescence microscope. The projected areas of 20 randomly selected adhered cells were measured using Image J software.

2.9.2.4. Measurement of intracellular Ca^{2+} concentration. It has been suggested that electrical stimulation activates the voltage-gated calcium channels and thereby, allowing a larger influx of extracellular Ca^{2+} to the cells which consequently, increases intracellular Ca^{2+} [3,37]. Such a rise in the concentration of intracellular Ca^{2+} promotes the transforming growth factor and bone morphogenetic protein through the activation of gene transcription [3,37]. Therefore, the external electrical stimulation induced augmentation in intracellular Ca^{2+} helps in regulating cellular metabolism. It has also been suggested that the intracellular Ca^{2+} are the second messenger responsible for optimal cellular functionality and bone remodeling [38,39,40,41]. In the present study, Fura-2 acetoxymethylester (Fura-2 AM, Thermofisher Scientific), an intracellular Ca^{2+} indicator dye was used which is based on the ratiometric method of measurement. In this experiment, the cells were seeded on the non-Pol. and polarized NKN and HA samples in 24 well plates, followed by the application of dynamic electrical stimulation (after 12 and 24 h). After 48 h of seeding, the culture media was removed and the samples were washed using HEPES buffered saline (HBS) solution, containing 1 mM $MgCl_2$, 5 mM KCl, 1 mM $CaCl_2$, 145 mM NaCl, 10 mM HEPES, 10 mM glucose (pH; 7.4). Thereafter, dye solution (containing HBS, 0.1 % BSA, 5 μM Fura-2 AM) was added to each sample and the samples were then incubated in dark. After 1 h, the dye solution was removed from each sample and washed with HBS. Following this, HBS solution,

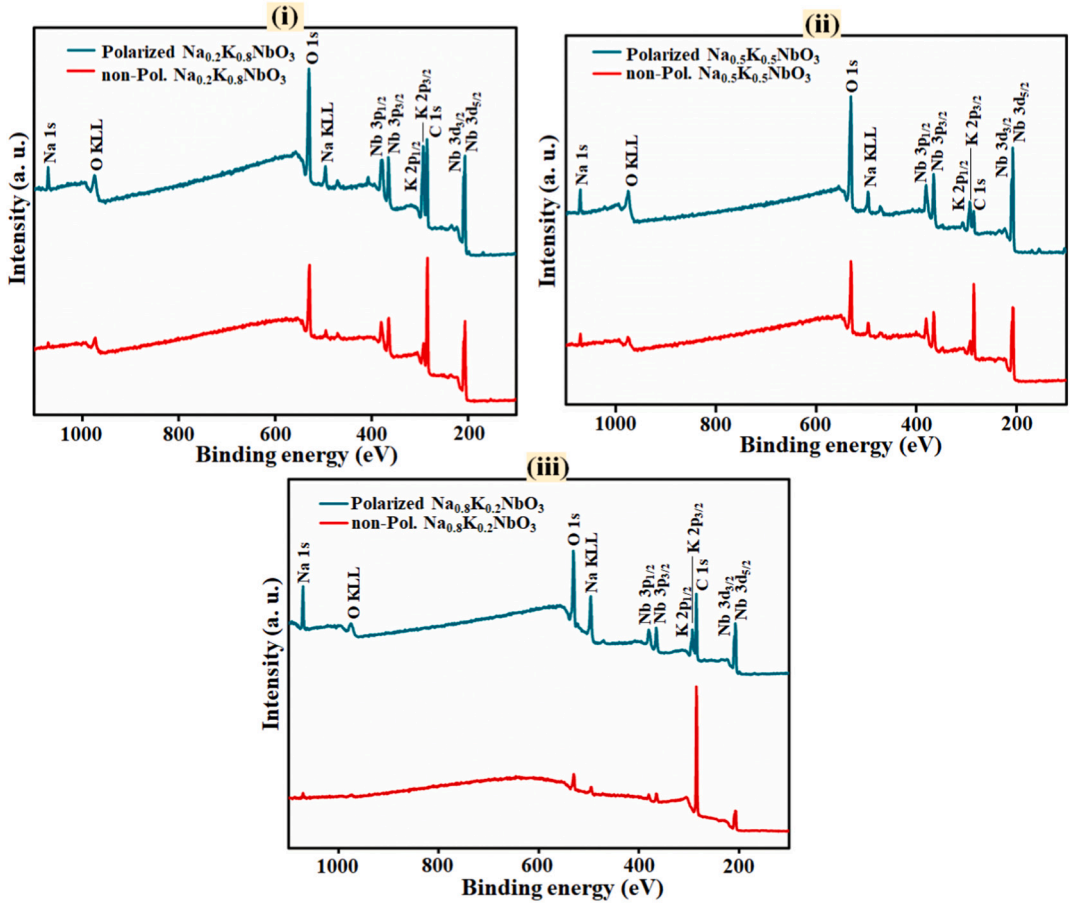

(a)

Fig. 7. XPS spectra for non-Pol. and polarized surfaces of $Na_xK_{1-x}NbO_3$ (x = 0.2, 0.5, 0.8) ceramics. (a) XPS survey specta of non-Pol. and polarized $Na_xK_{1-x}NbO_3$ (i) x = 0.2, (ii) x = 0.5, (iii) x = 0.8 for Na (1s), K (2p), Nb (3p), Nb (3d), C (1s) and O (1s) orbitals states. (b) Representation of the O 1 s XPS spectra for non-Pol. and polarized $Na_xK_{1-x}NbO_3$ (i) x = 0.2, (ii) x = 0.5, (iii) x = 0.8 samples.

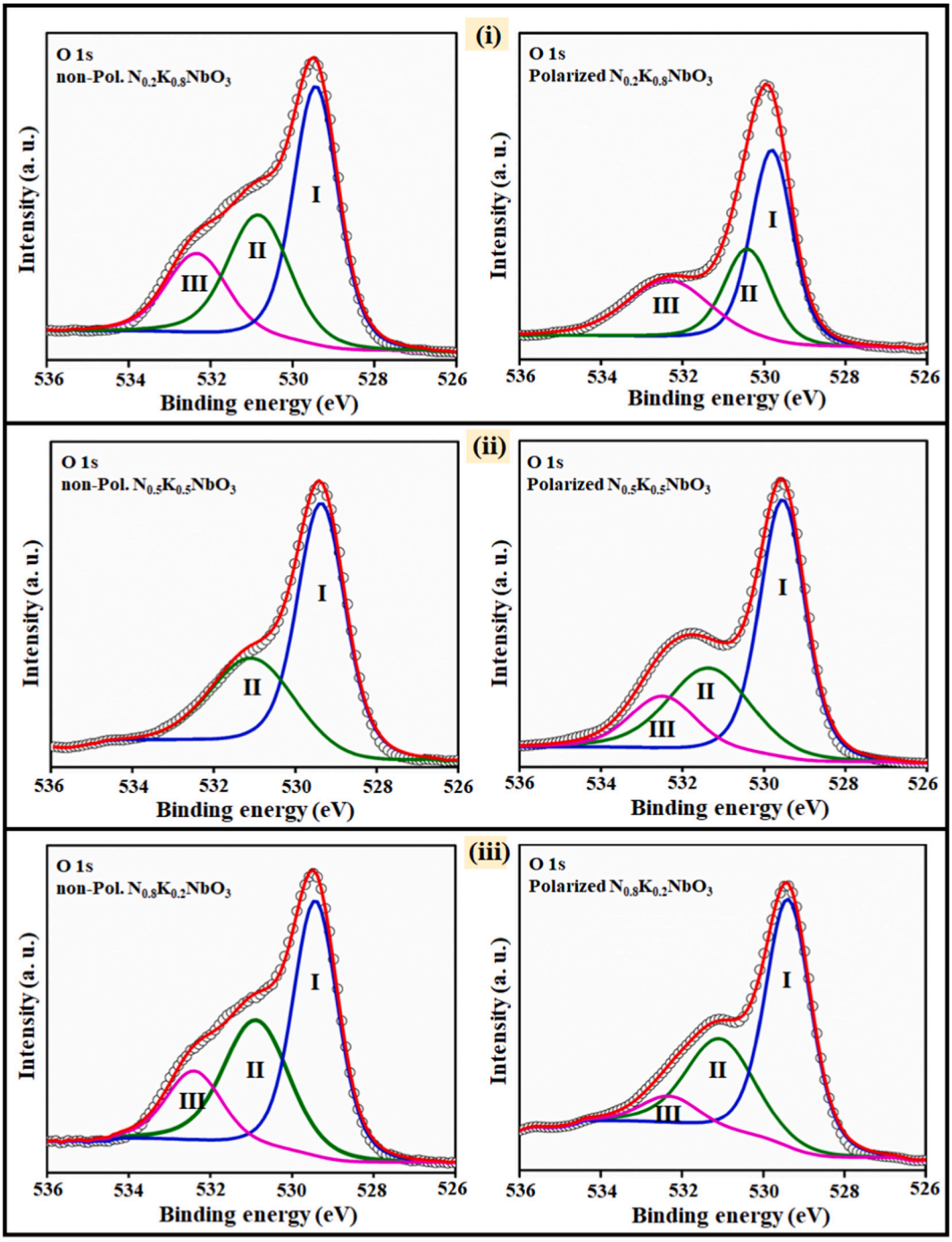

(b)

Fig. 7. (*continued*).

supplemented with probenecid (2.5 mM) was added to each sample and incubated for 20 min. in dark. Probenecid prevents the leakage of Fura-2 AM dye from the cells [42]. The solution from each well was transferred to the black colored 96 well plate and the reading was taken at the emission intensity of 510 nm. The excitation intensity was set at 340 and 380 nm as Fura-2 AM dye gives maximum fluorescence emission intensity with and without intracellular Ca^{2+} at the excitation wavelengths of 340 and 380 nm, respectively. Therefore, the ratio of the measured fluorescence intensity of Fura-2 AM at the excitation wavelengths of 340 (calcium bound) and 380 nm (calcium free) is directly proportional to the amount of intracellular calcium ions. The reading was taken at the interval of 10 s for 10 cycles using a fluorescence plate reader (Synergy H1).

3. Results

3.1. Structural analyses

The XRD spectra for sintered $Na_xK_{1-x}NbO_3$ (x = 0.2, 0.5, 0.8) samples demonstrate the monoclinic structure with space group P1m1 [JCPDS #

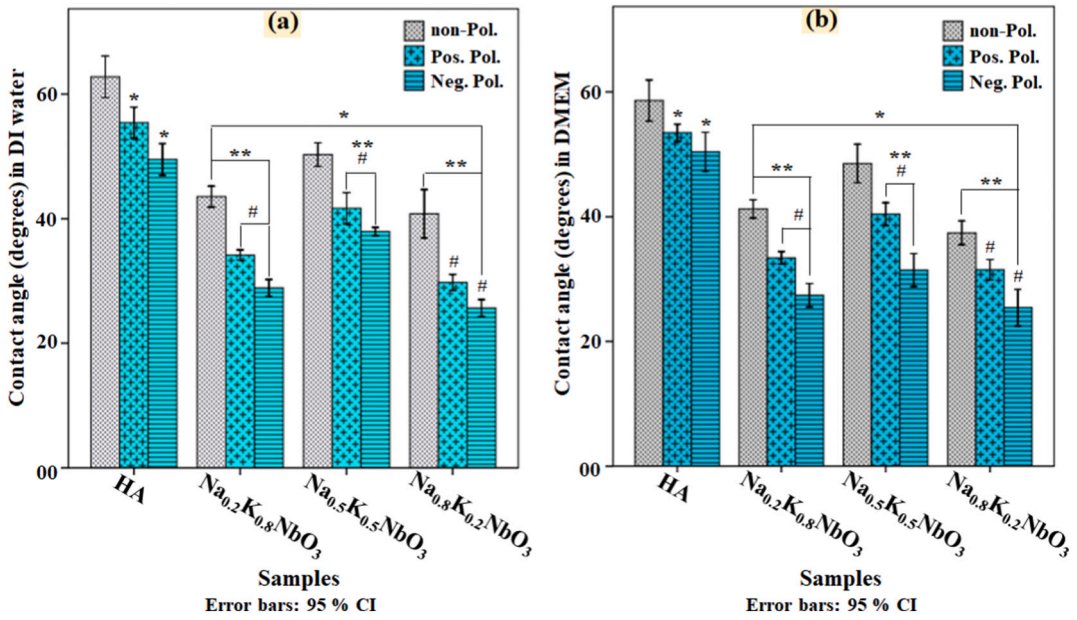

Fig. 8. Influence of surface polarization charge on hydrophilicity. The contact angle (°) values for non-Pol. and polarized surfaces of $Na_xK_{1-x}NbO_3$ (x = 0.2, 0.5, 0.8) and HA in (a) DI water and (b) DMEM media. (*) mark indicates the significant difference at $p \leq 0.05$, among the mean values of water contact angle on non-Pol. / polarized NKN and polarized HA samples in comparison to non-Pol. HA. (**) and (#) marks indicate the significant difference at $p \leq 0.05$, among the mean values of water contact angle on polarized NKN samples in comparison to Neg. Pol. HA and corresponding non-Pol. NKN samples, respectively.

77-0038] [17]. XRD patterns were analyzed using the Rietveld refinement technique to investigate the structural changes in $Na_xK_{1-x}NbO_3$ after compositional (x) variation. All the refinements were made by shift correction against reference monoclinic NKN. Pseudo-Voigt function was used for peak profile refinement. The X-ray diffraction data were plotted in conjunction with Rietveld refinement fitting [Fig. 2]. It indicates that the refined patterns are in well agreement with the observed patterns. The finally obtained values of refined parameters such as profile factor (R_p), expected weighted profile factor (R_{exp}), weighted profile factor (R_{wp}), and Bragg's factor (R) are listed in Table 1. The values of the goodness of fit (GOF) for $Na_xK_{1-x}NbO_3$ (x = 0.2, 0.5, 0.8) are 1.10, 1.05 and 1.02, which reflects an agreement between the theoretical and experimental data. In addition, the values of R_p, R_{wp} and R_{exp} further indicate good refinement.

3.2. Crystallite size and strain measurement

From the diffraction data (Fig. 2), the crystallite size and strain have been calculated using Scherrer, modified Scherrer, Williamson-Hall plot and size-strain plot. The crystallite size has been obtained using the Scherrer formula (Eq. (3)) for $Na_xK_{1-x}NbO_3$ ceramic samples (Table 2) as:

$$D = \frac{k\lambda}{\beta cos\theta} \tag{3}$$

where, *D, β, λ, k* and *θ* are crystallite size (in nm), FWHM (in radians), the wavelength of X-ray (1.54046 Å), shape factor (0.94) and Bragg's diffraction angle (in radians), respectively.

The modified Scherrer method considers each peak during the measurement of crystallite size and therefore, reduced the error in measurements. By taking $\log_e$ on both sides of Eq. (3), we get,

$$ln\beta = ln\left(\frac{k\lambda}{D}\right) + ln\left(\frac{1}{cos\theta}\right) \tag{4}$$

By plotting a graph between ln (1/cos θ) along x-axis and ln (β) along y-axis, the crystallite size can be calculated from the intercept (ln *kλ/D*) [Fig. 3 (a)].

Due to the deduction of errors, the obtained value of crystallite size from the modified Scherrer method is higher than the value, measured using the Scherrer method (Table 2).

Williamson Hall plot is an integral breadth method which considers peak width as a function of diffraction angle (2θ) [43]. Apart from the size of the crystallites, the XRD pattern is also influenced by the lattice strain. This model assumes NKN material as isotropic and the strain distribution is uniform in all the directions. It clearly demonstrates the size and strain-induced deformation with considerable peak broadening. Therefore, total peak broadening will be the sum of the size and strain-induced broadening of peaks [44].

Therefore:

$$\beta = \beta_D + \beta_\varepsilon \tag{5}$$

$$\beta cos\theta = \left(\frac{k\lambda}{D}\right) + 4\varepsilon sin\theta \tag{6}$$

where, D and ε represent the values of crystallite size and lattice strain, respectively.

The intercept (kλ/D) and slope provide the crystallite size (D) and strain (ε) for $Na_xK_{1-x}NbO_3$ ceramic samples [Fig. 3 (b)].

Size-strain plot method is more accurate as it preferentially considers the low angle values of XRD reflection peaks where, the XRD data are more accurate and precise than those of the high angle values [45,46]. In this method, Lorentz and Gaussian functions illustrate the profiles of crystallite size and strain, respectively [45,46,47]. Therefore, the total broadening of the size-strain plot is the sum of Lorentz and Gaussian functions i.e., $\beta = \beta_L + \beta_G$, where, β_L and β_G are the broadening of peaks for Lorentz and Gaussian functions, respectively.

According to the size-strain plot method,

$$(d\beta cos\theta)^2 = \left(\frac{k\lambda}{D}\right)(d^2\beta cos\theta) + \left(\frac{\varepsilon}{2}\right)^2 \tag{7}$$

where, d is interplanar spacing.

The intercept $[(\varepsilon/2)^2]$ and slope (kλ/D) can be used to calculate the crystallite size and strain for $Na_xK_{1-x}NbO_3$ samples, respectively [Fig. 3 (c)].

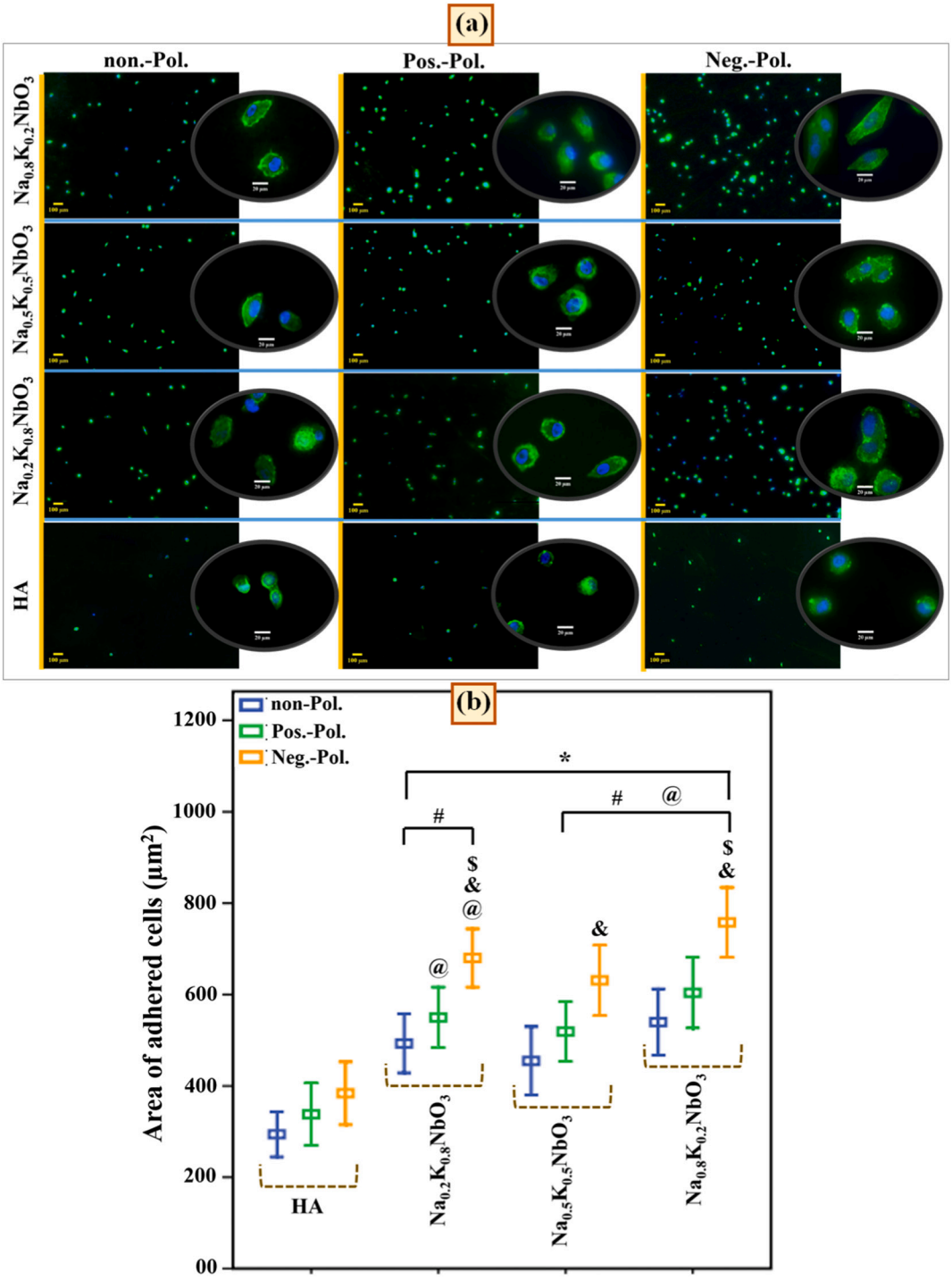

Fig. 9. Influence of polarization on early-stage adhesion (after 6 h) of MG-63 cells. (a) The representative florescence images of MG-63 cells, adhered on non-Pol. and polarized $Na_xK_{1-x}NbO_3$ and control samples. (b) The plot, representing the projected area of the adhered cells ($n = 20$), on the non-Pol. and polarized NKN and control samples. (*), (#) and (@) marks indicate the significant difference at $p \leq 0.05$, among the mean projected area of adhered cells on the non-Pol. and polarized $Na_xK_{1-x}NbO_3$ samples in comparison to the non-Pol., Pos. Pol. and Neg. Pol. control, respectively. (&) and ($) marks indicate the significant difference at $p \leq 0.05$, among the mean projected area of cells, adhered on the Neg. Pol. $Na_xK_{1-x}NbO_3$ samples in comparison to their respective non-Pol. and Pos. Pol. NKN samples, respectively.

The results of crystallite sizes and/or lattice strain for $Na_xK_{1-x}NbO_3$ ($x = 0.2, 0.5, 0.8$) samples, obtained from different methods are summarized in Table 2.

Among various methods, the size-strain plot method provides more accurate data of crystallite size and lattice strain than the Williamson-Hall plot, Scherrer and modified Scherrer methods as the high-intensity points lie more close to the linear fit. Bragg's angle of the most intense peaks shifted towards the higher angle values from $Na_{0.2}K_{0.8}NbO_3$ to $Na_{0.5}K_{0.5}NbO_3$, which may be due to the larger crystallite size of $Na_{0.5}K_{0.5}NbO_3$ sample [17]. However, X-ray peak profile analyses, using different methods, are revealing a comparatively smaller crystallite size of $Na_{0.8}K_{0.2}NbO_3$ than $Na_{0.5}K_{0.5}NbO_3$. From $Na_{0.5}K_{0.5}NbO_3$ to $Na_{0.8}K_{0.2}NbO_3$, the K content decreases which has a comparatively larger ionic radius than Na [48,49]. It may be the reason

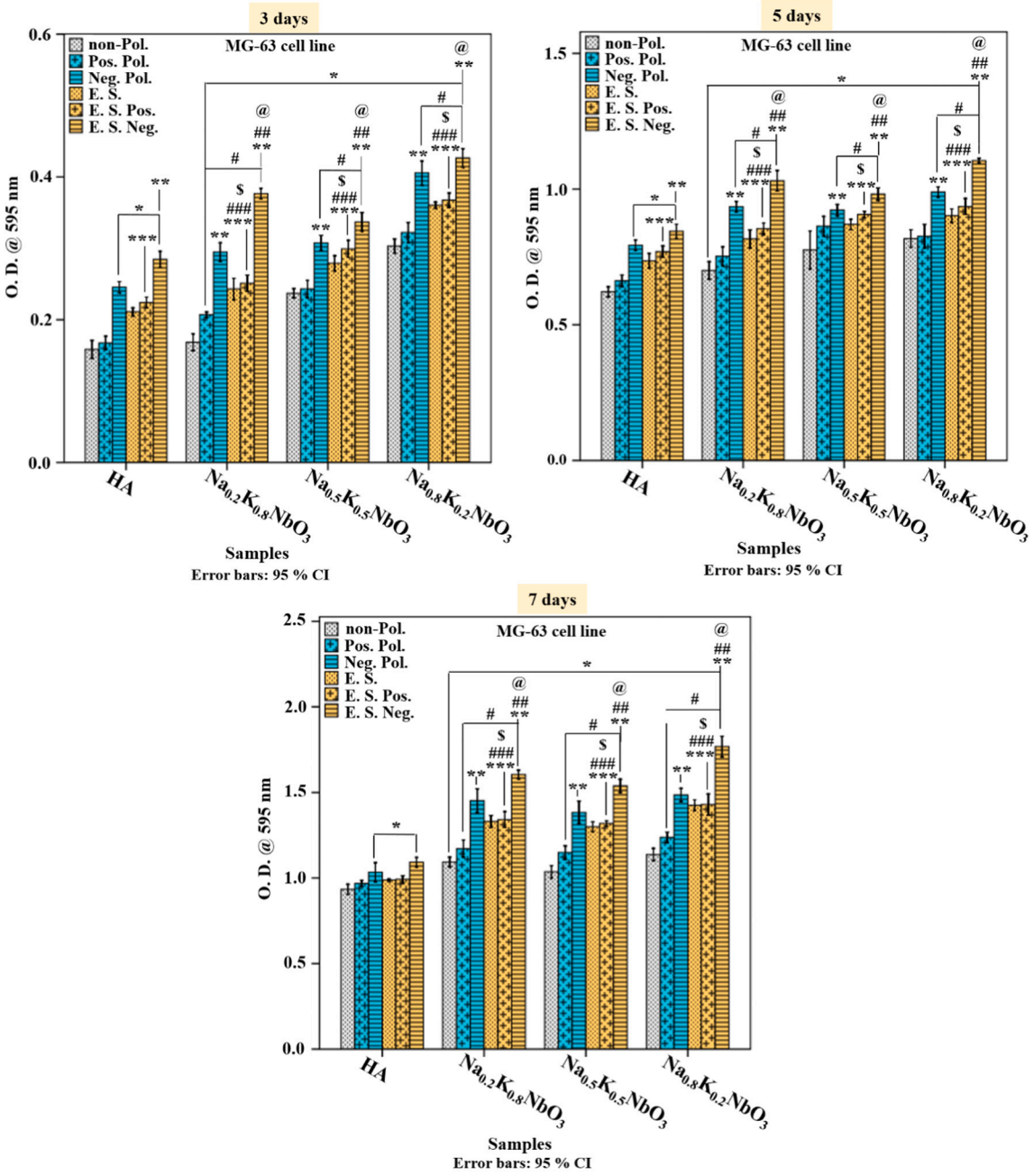

(a)

Fig. 10. Quantitative cellular response on non-treated and treated NKN and control samples. The plots representing the quantitative cellular response, using (a) MG-63 cells and (b) hMSCs, on non-Pol. and polarized $Na_xK_{1-x}NbO_3$ (x = 0.2, 0.5, 08) and control samples in absence and presence of dynamic pulsed electrical stimulation. (*) mark indicates the significant difference at $p \leq 0.05$, among the mean values of optical density (O. D.) on all the non-treated and treated (Electrostatic/dynamic pulsed electrical stimulation) NKN and HA samples in comparison to non-Pol. HA, (#) mark denotes the significant difference at $p \leq 0.05$, among the mean values of O. D. on all the treated NKN samples in comparison to their respective non-Pol. NKN samples, (**) mark indicates the significant difference at $p \leq 0.05$, among the mean values of O. D. on Neg. Pol. NKN, electrically stimulated Neg. Pol. (E. S. Neg.) NKN and E. S. Neg. HA samples in comparison to Neg. Pol. HA. (##) and (@) symbols indicate the significant difference at $p \leq 0.05$, among the mean values of O. D. on E. S. Neg. NKN samples in comparison to their corresponding Neg. Pol. NKN and E. S. Neg. HA samples, respectively. (***) mark denotes the significant difference at $p \leq 0.05$, among the mean values of O. D. on the electrically stimulated Pos. Pol. (E. S. Pos.) NKN and HA samples in comparison to Pos. Pol. HA samples. (###) and ($) symbols indicate the significant difference at $p \leq 0.05$, among the mean values of O. D. on E. S. Pos. NKN samples in comparison to their corresponding Pos. Pol. NKN and E. S. Pos. HA samples, respectively.

for the smaller crystallite size of $Na_{0.8}K_{0.2}NbO_3$ than $Na_{0.5}K_{0.5}NbO_3$.

Among three compositions of $Na_xK_{1-x}NbO_3$ (x = 0.2, 0.5 and 0.8), Williamson-Hall methods demonstrated comparatively higher value of lattice strain for $Na_{0.5}K_{0.5}NbO_3$ than $Na_{0.2}K_{0.8}NbO_3$ and $Na_{0.8}K_{0.2}NbO_3$ samples (Table 2). Similarly, the size-strain plot method is also revealing a higher value of lattice strain for $Na_{0.5}K_{0.5}NbO_3$ sample than for $Na_{0.2}K_{0.8}NbO_3$. However, the size-strain plot method is demonstrating a negative intercept for $Na_{0.8}K_{0.2}NbO_3$ sample and therefore, the

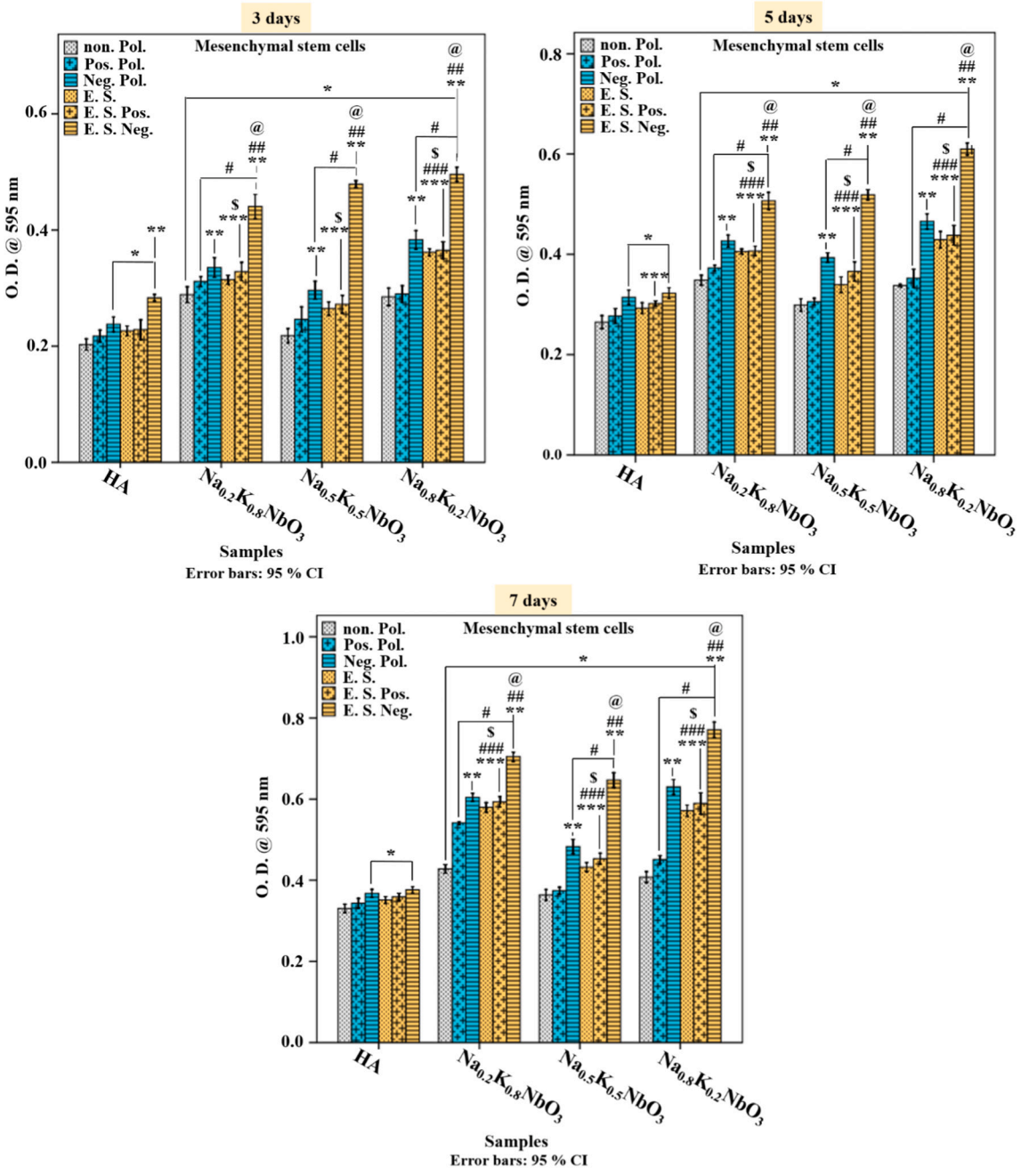

(b)

Fig. 10. (*continued*).

measurement of lattice strain is not possible in this case [50]. The higher value of lattice strain for $Na_{0.5}K_{0.5}NbO_3$ may be due to the presence of lattice distortion, dislocations, oxygen deficiency or sintering stress [51,52,53]. In addition, lattice strain may also occur due to the lattice contraction or expansion [54].

3.3. Mechanical properties

Vicker's hardness and compressive strength were measured for sintered $Na_xK_{1-x}NbO_3$ (x = 0.2, 0.5, 0.8) and HA samples [Fig. 4]. The hardness values for $Na_{0.2}K_{0.8}NbO_3$, $Na_{0.5}K_{0.5}NbO_3$ and $Na_{0.8}K_{0.2}NbO_3$ are 5.8 ± 0.4, 6.5 ± 0.3 and 6.8 ± 0.4 GPa, respectively. However, the hardness value for HA sample is comparatively lower (4.7 ± 0.4 GPa). The human bone has hardness value of (0.4–0.76 GPa) [55,56,57]. The maximum compressive strengths for $Na_{0.2}K_{0.8}NbO_3$, $Na_{0.5}K_{0.5}NbO_3$ and $Na_{0.8}K_{0.2}NbO_3$ are 121.73 ± 5.27, 128.05 ± 4.55 and 136.47 ± 5.86 MPa, respectively, which are comparatively higher than that of HA (81.65 ± 4.44 MPa) samples. The compressive strength for NKN samples is comparable to that of human bone (131 ± 20.7) MPa [58,59]. The favorable mechanical properties reveal the potentiality of NKN ceramic to be used as a robust implant material.

3.4. Leaching behavior

The ionic concentrations of Na^+ and K^+, leached from $Na_xK_{1-x}NbO_3$ (x = 0.2, 0.5, 0.8) after 7, 14 and 21 days of the immersion in SBF, are

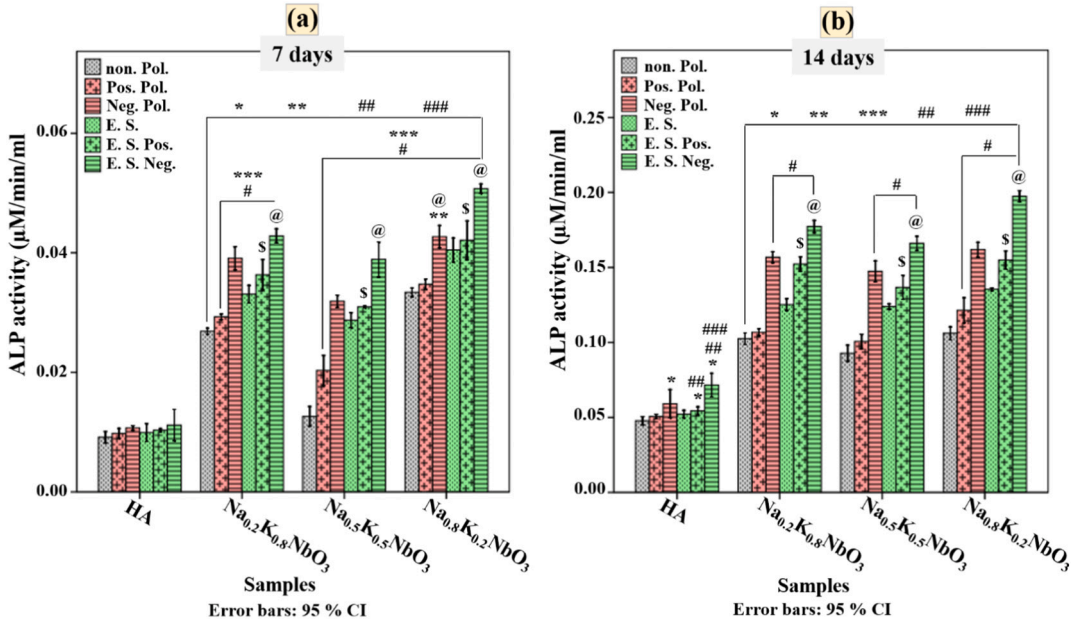

Fig. 11. Osteogenic differentiation response of non-treated and treated piezoelectric NKN and control samples. The plot illustrating the alkaline phosphatase (ALP) activity on the non-Pol., electrostatically (Pos. and Neg. Pol.) – electrically stimulated (dynamic) Pos. Pol. (E. S. Pos.) and electrically stimulated (dynamic) Neg. Pol. (E. S. Neg.) $Na_xK_{1-x}NbO_3$ (x = 0.2, 0.5, 0.8) and HA samples, after (a) 7 and (b) 14 days. (*), (##), (###) symbols indicate the significant difference at $p \leq 0.05$, among the mean ALP activity on all of the non-treated and treated NKN and HA samples in comparison to non-Pol., Pos. Pol. and E. S. Pos. HA samples, respectively. (**), (***) symbols indicate the significant difference at $p \leq 0.05$, among the mean ALP activity on all of the NKN samples in comparison to Neg. Pol. and E. S. Neg. HA, respectively. (#) mark indicates the significant difference at $p \leq 0.05$, among the mean ALP activity on all of the treated NKN samples in comparison to their corresponding non-Pol. NKN samples. (@) mark indicates the significant difference at $p \leq 0.05$, among the mean ALP activity on all of the E. S. Neg. NKN samples in comparison to their respective Neg. Pol. NKN. ($) mark indicates the significant difference at $p \leq 0.05$, among the mean ALP activity on all of the E. S. Pos. NKN samples in comparison to their corresponding Pos. Pol. NKN samples, respectively.

illustrated in Fig. 5. For Na-rich (i.e., $Na_{0.8}K_{0.2}NbO_3$) and K-rich (i.e., $Na_{0.2}K_{0.8}NbO_3$) samples, the leaching of Na^+ and K^+ initially increases up to 7 days and decreases thereafter. However, no significant leaching of these ions is observed in the composition with similar Na and K contents (i.e., $Na_{0.5}K_{0.5}NbO_3$). The maximum amount of leached Na^+ and K^+ for Na and K-rich compositions i.e., $Na_{0.8}K_{0.2}NbO_3$ and $Na_{0.2}K_{0.8}NbO_3$ are (Na^+: 608 ppm, K^+: 261 ppm) and (Na^+: 504 ppm, K^+: 400 ppm), respectively. However, this value for $Na_{0.5}K_{0.5}NbO_3$ is (Na^+: 445 ppm, K^+: 215 ppm).

3.5. Charge measurement

The polarization induced surface charge on the $Na_xK_{1-x}NbO_3$ samples were measured from thermally stimulated depolarized current (TSDC) plot [Fig. 6] as [10]:

$$Q = \frac{1}{\beta}\int 1(T)dT \tag{8}$$

where, I, β and T are the current, heating rate (5 °C/min.) and temperature, respectively. The calculated surface charge densities for $Na_xK_{1-x}NbO_3$ (x = 0.2, 0.5, 0.8) samples are 0.515, 0.498 and 0.465 μC/cm^2, respectively.

The $Na_xK_{1-x}NbO_3$ exhibits the transitions of cubic to tetragonal ($T_{C\text{-}T}$, Curie point) and monoclinic to tetragonal ($T_{M\text{-}T}$) phase, at temperatures of ~420 and ~210, respectively [49,60,61]. In our study, the TSDC spectra reveal the Curie point temperatures for $Na_xK_{1-x}NbO_3$ (x = 0.2, 0.5, 0.8) samples to be 425, 417 and 410 °C, respectively. Moreover, the lower temperature phase transition is detected at the temperatures of 235, 229 and 221 °C, respectively. Interestingly, a slight shift in phase transition temperatures towards the higher temperature region is observed with increasing the content of K which is in agreement with the previous study, performed for sodium potassium niobates mixed ceramic system [49].

3.6. X-ray photoelectron spectroscopy (XPS) analyses

In XPS, the survey spectra demonstrate the binding energies of five elements on the surfaces of non-Pol. and polarized $Na_xK_{1-x}NbO_3$ (x = 0.2, 0.5, 0.8) samples i.e., Na (1s), K (2p), Nb (3p and 3d), C (1s) and O (1s) are shown in Figs. 7 (a) and (b). The peaks of binding energies for C 1s and Na 1s are observed at about 285.1 eV and 1071.1 eV, respectively, for both, non-Pol. and polarized samples. The binding energy peaks, corresponding to K 2p, Nb 3p and Nb 3d were deconvoluted to ($2p_{1/2}$, $2p_{3/2}$), ($3p_{1/2}$, $3p_{3/2}$) and ($3d_{3/2}$, $3d_{5/2}$), which are found to be at about (295.1, 293.1), (380.08, 365.08) and (209.1, 206.5 eV), respectively, for both, non-Pol. and polarized samples of $Na_xK_{1-x}NbO_3$. The binding energies of the observed orbitals C 1s, Na 1s, K 2p, Nb 3p and Nb 3d for non-Pol. and polarized NKN samples are close to the reported values for NKN [62,63,64]. The XPS spectra also reveal the Auger features of Na KLL and O KLL for non-Pol. and polarized $Na_xK_{1-x}NbO_3$ samples [Fig. 7 (a)] [64].

The XPS spectra of O 1s orbital scan for non-Pol. and polarized $Na_xK_{1-x}NbO_3$ (x = 0.2, 0.5, 0.8) samples are illustrated in Fig. 7 (b). The O 1 s peaks for $Na_xK_{1-x}NbO_3$ are deconvoluted into two or three peaks, centered at about 529.5 eV [O 1s (I): Curve I], 531 eV [O 1s (II): Curve II] and 532.4 eV [O 1s (III): Curve III]. It has been reported that the highest intense peak (curve I) is attributed to the presence of oxygen in the lattice state i.e., Nb—O bond in NKN ceramic [53,65]. However, another peak (curve II) corresponds to the presence of oxygen vacancy [62,66,67,68,69,70,71]. The additional small peak at the higher binding energy side (Curve III) is assigned to the adsorbed CO_2 or oxygen [53,67,69,72,73]. It can be clearly seen that the peak area, corresponding to the oxygen vacancy [O 1s (II)] for the polarized $Na_xK_{1-x}NbO_3$ sample are larger than non-Pol. counter-part. Further, the ratios of the area under the curves representing the oxygen in the lattice (curve I) and oxygen vacancy (curve II), calculated for non-Pol. and polarized samples are (1.83, 1.55), (1.84, 1.69) and (1.83, 1.43) for

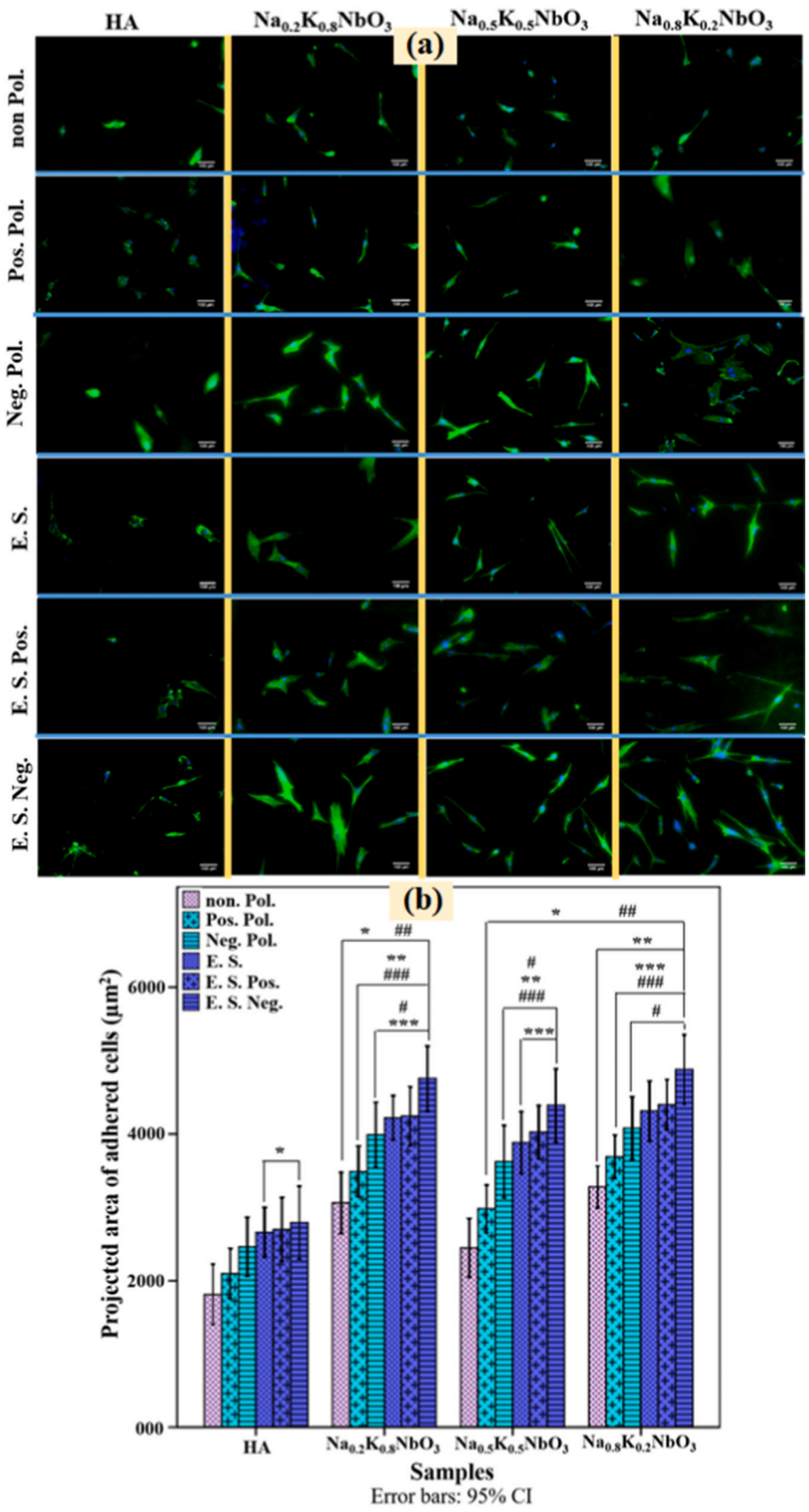

Fig. 12. Morphological analyses of adhered cells on non-treated and treated NKN and control samples. (a) Representative fluorescence microscopic images of stained hMSCs, adhered on the non-treated and treated (Electrostatically/dynamically stimulated) piezoelectric $Na_xK_{1-x}NbO_3$ samples and control. (b) The plot represents the projected area of the adhered cells ($n = 20$) on non-treated and treated NKN samples and control. (*), (##), (###) symbols indicate the significant difference at $p \leq 0.05$, among the mean projected area of cells adhered on all of the non-treated and treated NKN and HA samples in comparison to non-Pol., Pos. Pol. and E. S. Pos. HA samples, respectively. (**), (***) symbols indicate the significant difference at $p \leq 0.05$, among the mean projected area of cells, adhered on all of the NKN samples in comparison to Neg. Pol. and E. S. Neg. HA, respectively. (#) symbol indicates the significant difference at $p \leq 0.05$, among the mean projected area of cells, adhered on all of the treated NKN samples in comparison to their respective non-Pol. NKN samples.

$Na_{0.2}K_{0.8}NbO_3$, $Na_{0.5}K_{0.5}NbO_3$, $Na_{0.8}K_{0.2}NbO_3$, respectively. The low area ratios are indicating the accumulation of oxygen vacancies on the polarized surface of $Na_xK_{1-x}NbO_3$ as compared to non-Pol. counter-part which are found to be comparatively higher for Na-rich NKN (i.e., $Na_{0.8}K_{0.2}NbO_3$) and K-rich NKN (i.e., $Na_{0.2}K_{0.8}NbO_3$) samples than $Na_{0.5}K_{0.5}NbO_3$. It has been reported that the oxygen vacancies induced active sites on the surface, facilitate the dissociative adsorption of water and therefore, make the surface hydrophilic [74,75,76,77]. Overall, high-resolution O1s spectra of polarized $Na_xK_{1-x}NbO_3$ reveals that the surface polarization enhanced the hydrophilicity, which augments the cellular functionality [78,79,80]. Apart from these results, the similar peak positions of Na, K and Nb for non-Pol. and polarized samples reveal

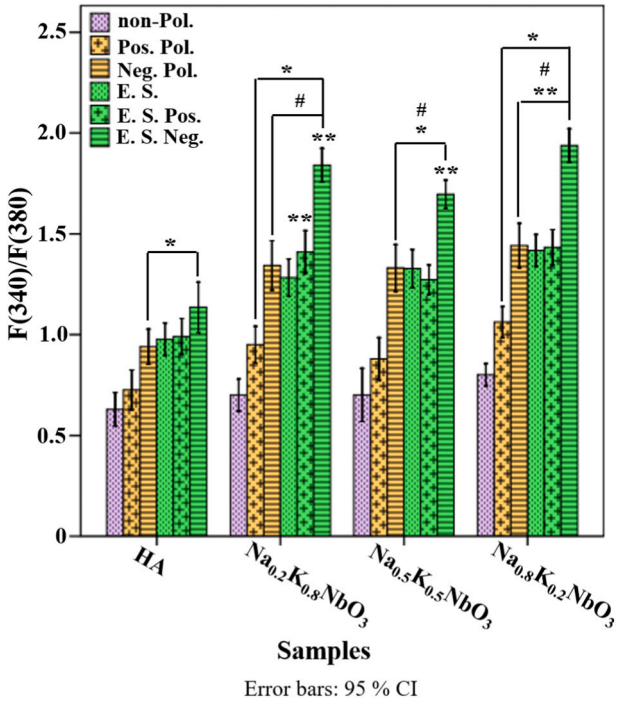

Fig. 13. The level of intracellular Ca^{2+} on non-treated and treated NKN and control samples, cultured with MG-63 cells. The plot representing the mean of the peak values of the ratio of fluorescence intensity at 340 and 380 nm, measured for the cells loaded with intracellular Ca^{2+} indicator Fura-2 AM on the non-treated and treated (Electrostatically/dynamically stimulated) piezoelectric $Na_xK_{1-x}NbO_3$ samples and control. (*) mark indicates the significant difference at $p \leq 0.05$, among the mean of peak values of estimated ratio on Neg. Pol., E. S., E. S. Pos. and E. S. Neg. NKN as well as HA samples, in comparison to non-Pol. and polarized HA samples, cultured without dynamic electrical stimulation. (**) mark indicates the significant difference at $p \leq 0.05$, among the mean of peak values of estimated ratio on Neg. Pol., E. S., E. S. Pos. and E. S. Neg. NKN samples, in comparison to non-Pol. and polarized HA samples, cultured with dynamic electrical stimulation. (#) mark indicates the same at $p \leq 0.05$, among non-Pol. and polarized NKN samples, cultured under dynamic electrical stimulation in comparison to their corresponding non-Pol. and polarized NKN samples, cultured without electrical stimulation.

that the polarization treatment did not alter the surface chemistry of the NKN sample.

3.7. Contact angle measurement

The influence of polarization charge on the surface wettability was assessed by the measurement of contact angle with DI water and DMEM media [Figs. 8 (a) and (b)]. The contact angles were observed to be significantly reduced on the polarized (both, positive and negative) surfaces of $Na_xK_{1-x}NbO_3$ (x = 0.2, 0.5, 0.8) and control samples, which indicates the polarization induced hydrophilicity. In addition, Neg. Pol. samples reveal the smallest contact angle i.e., highest hydrophilicity as compared to Pos. Pol. and non-Pol. samples. For Neg. Pol. $Na_xK_{1-x}NbO_3$ (x = 0.2, 0.5, 0.8) surfaces, the contact angle reduced by 54, 40, 59 % than that of the non-Pol. HA. Whereas, the Neg. Pol. surface of HA sample shows comparatively small reduction in contact angle (21 % than that of the non-Pol. HA), as measured in DI water. A similar trend is observed in DMEM media, where the contact angles on the Neg. Pol. surfaces of $Na_xK_{1-x}NbO_3$ (x = 0.2, 0.5, 0.8) samples are reduced by 53, 46, 57 % than that of the non-Pol. HA. However, Neg. Pol. surface of HA demonstrates only 14 % reduction than that of the non-Pol. HA. Among all three Neg. Pol. NKN samples, Na and K-rich NKN i.e., $Na_{0.8}K_{0.2}NbO_3$ and $Na_{0.2}K_{0.8}NbO_3$ compositions are revealing comparatively higher hydrophilicity than $Na_xK_{1-x}NbO_3$ (x = 0.5). The hydrophilic surfaces are more favorable for cellular growth and proliferation as compared to hydrophobic surfaces [9,78,80]. The contact angle measurement demonstrates enhanced hydrophilicity of the polarized surfaces of $Na_xK_{1-x}NbO_3$ as compared to non-Pol. surfaces, which is in well agreement with the outcomes of XPS analyses.

3.8. Cellular response

3.8.1. Polarization induced early-stage cell adhesion

The fluorescence images of osteoblast-like MG-63 cells, adhered on non-Pol. and polarized $Na_xK_{1-x}NbO_3$ and HA control, after 6 h of incubation, are shown in Fig. 9. The cells, adhered on the NKN samples, are found to be more flattened and elongated than those on the HA samples. In addition, the polarized surfaces of NKN and control samples are observed to reveal larger-sized adhered cells than their non-Pol. counterpart [Fig. 9 (a)]. The statistical analyses demonstrate that the cells, adhered on the Neg. Pol. $Na_xK_{1-x}NbO_3$ samples are significantly larger in size than those on the non-Pol. and polarized HA samples as well as their corresponding non-Pol. NKN samples [Fig. 9 (b)]. The mean projected area of the cells, adhered on the Neg. Pol. $Na_xK_{1-x}NbO_3$ (x = 0.2, 0.5, 0.8) samples are measured to be 2.3, 2.1, 2.6 times higher than those on the non-Pol. HA. In addition, Pos. Pol. and non-Pol. $Na_xK_{1-x}NbO_3$ (x = 0.2, 0.5, 0.8) samples reveal the mean projected area of adhered cells as (1.9, 1.8, 2.1 times of non-Pol. HA) and (1.7, 1.5, 1.8 times of non-Pol. HA), respectively. However, no significant difference in the projected area of adhered cells is observed in non-Pol., Pos. Pol. and Neg. Pol. HA samples. Among different compositions of NKN, Neg. Pol. Na-rich NKN i.e., $Na_{0.8}K_{0.2}NbO_3$ and K-rich NKN i.e., $Na_{0.2}K_{0.8}NbO_3$ samples, not only exhibit comparatively larger projected area of adhered cells than Neg. Pol. $Na_{0.5}K_{0.5}NbO_3$, but also demonstrated a significant increase in the projected area of adhered cells than their respective Pos. Pol. NKN samples [Fig. 9 (b)]. However, no significant difference is observed among the projected area of adhered cells on Neg. and Pos. Pol. surfaces of $Na_{0.5}K_{0.5}NbO_3$. Overall, this result demonstrates that surface polarization accelerates the early-stage adhesion of cells, preferably on the Neg. Pol. surfaces of Na and K-rich compositions of NKN.

3.8.2. Combined effect of surface polarization and dynamic electrical stimulation

The synergistic contribution of surface polarization charge and dynamic pulsed electrical stimulation on the osteogenic response of piezoelectric $Na_xK_{1-x}NbO_3$ (x = 0.2, 0.5, 0.8) samples and HA control have been assessed using MTT assay, ALP activity, fluorescence imaging and intracellular calcium ions measurement.

3.8.2.1. MTT assay. The viability of MG-63 cells and hMSCs on the non-treated and electrostatic and dynamic pulsed electric field treated $Na_xK_{1-x}NbO_3$ samples and control were quantitatively measured in terms of cell proliferation [Fig. 10]. Irrespective of any treatment, the cell viability is observed to increase as the incubation period increases, for all the examined compositions. The treated NKN samples are demonstrating significantly higher viability for both of the cells as compared to treated HA samples, throughout the incubation period of 7 days. The Neg. Pol. $Na_xK_{1-x}NbO_3$ samples are revealing higher viability of MG-63 cells and hMSCs than their corresponding non-Pol. and Pos. Pol. NKN samples after 3, 5 and 7 days of incubation. This result is consistent with the results, obtained from the previous section (Section 3.8.1). Interestingly, after 7 days of incubation, the dynamic pulsed electrical stimulation significantly enhances the viability, while the cells are being adhered on the charged NKN samples as compared to the cellular response on merely charged surfaces [Figs. 10 (a) and (b)]. Overall, it can be clearly observed that the synergistically (electrostatic and dynamic electric field) treated NKN samples are showing maximum viability for both, MG-63 cells and hMSCs, throughout the study period. Among different compositions of NKN, the viability of MG-63 cells on

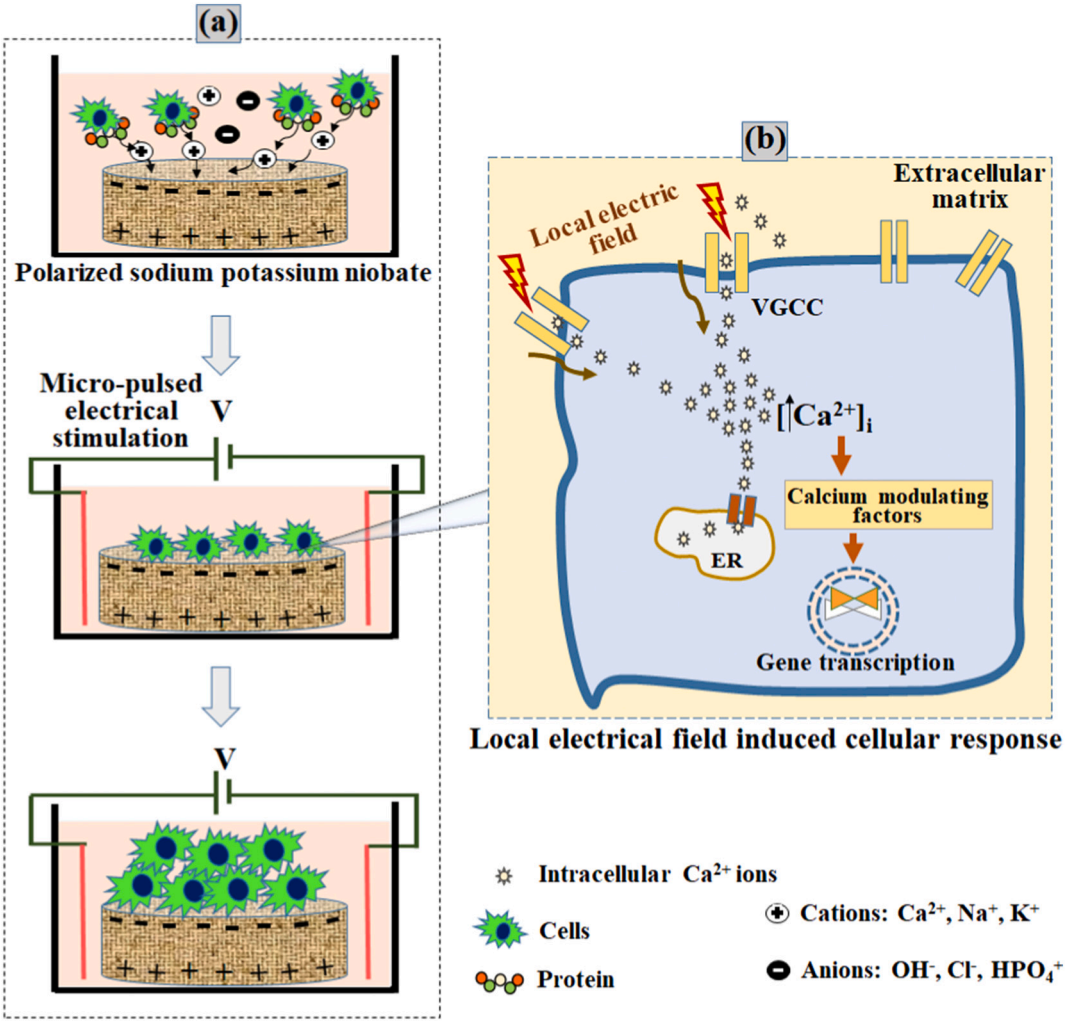

Fig. 14. Schematic demonstrating the synergized effect of Neg. Pol. surface and dynamic pulsed electrical stimulation in promoting cellular response of piezoelectric NKN. (a) The cations present in the culture media attract towards the Neg. Pol. surface and thereby, the adhered cations further attracted negatively charged cell membrane and protein and consequently, promote cellular adhesion [3,37]. In addition, hydrophilicity increases for the Neg. Pol. surface, which consequently, accelerates cellular functionality [9]. (b) The piezoelectric charge and dynamic pulsed electrical stimulation induced local electric field activates the voltage gated Ca^{2+} channels which permits the influx of Ca^{2+} [3,37]. The increased concentration of intracellular Ca^{2+} activates the calcium modulating factors which further results in gene transcription and therefore, assists in regulating cellular metabolism [3,37].

the Neg. Pol. and electrically stimulated Neg. Pol. (E. S. Neg.) surfaces of $Na_xK_{1-x}NbO_3$ (x = 0.2, 0.5, 0.8) samples are measured to be (156, 148, 160 % of non-Pol. HA samples) and (172, 165, 190 % of non-Pol. HA samples), respectively, after 7 days of incubation. However, the viabilities of hMSCs are measured to be (183, 146, 191 % of non-Pol. HA samples) and (213, 196, 234 % of non-Pol. HA samples) on the Neg. Pol. and E. S. Neg. $Na_xK_{1-x}NbO_3$ (x = 0.2, 0.5, 0.8) samples, respectively, for the similar incubation period. It can be clearly seen that E. S. Neg. Na-rich NKN i.e., $Na_{0.8}K_{0.2}NbO_3$ and K-rich NKN i.e., $Na_{0.2}K_{0.8}NbO_3$ are showing the highest viability of MG-63 cells and hMSCs than $Na_{0.5}K_{0.5}NbO_3$ samples, after 7 days of incubation.

3.8.2.2. ALP activity assessment. The ALP activity of MG-63 cells on non-treated and treated (Electrostatically/dynamically stimulated) piezoelectric $Na_xK_{1-x}NbO_3$ samples and control is represented in Fig. 11. After 7 days of incubation, the measured ALP activities are observed to be significantly higher on all of the non-treated and treated NKN samples (except non-Pol. $Na_{0.5}K_{0.5}NbO_3$) as compared to non-treated as well as treated HA control [Fig. 11 (a)]. However, after 14 days of cell seeding, entire examined compositions of NKN (irrespective of treatment methods) exhibit a significant increase in ALP activity with MG-63 cells [Fig. 11 (b)]. It can be clearly seen that the Neg. Pol. NKN samples are representing significantly higher ALP activities than the Pos. Pol. as well as non-Pol. surfaces of their respective compositions of NKN. Interestingly, the application of dynamic pulsed electrical stimulation over polarized surfaces further enhanced the ALP activity and consequently, resulted in a significant increase in the ALP activity as compared to the respective polarized NKN samples, cultured in the absence of electrical stimulation [Figs. 11 (a) and (b)]. The maximum ALP activity is observed on the electrically stimulated Neg. Pol. (E. S. Neg.) NKN samples, among all of the non-treated and treated samples. This finding indicates that the synergistic action of electrostatic-dynamic electrical stimulation considerably promoted earlier differentiation of osteoblast-like MG-63 cells. After 14 days of cell seeding, the values of ALP activity on the Neg. Pol. and E. S. Neg. $Na_xK_{1-x}NbO_3$ (x = 0.2, 0.5, 0.8) samples are measured to be (3.28, 3.08, 3.38 times of non-Pol. HA) and (3.71, 3.47, 4.13 times of non-Pol. HA), respectively. However, these values on the Neg. Pol. and E. S. Neg. HA samples are (1.27 times of non-Pol. HA) and (1.51 times of non-Pol. HA), respectively. From the above results, it can be seen that E. S. Neg. Na-rich NKN i.e., $Na_{0.8}K_{0.2}NbO_3$ and K-rich NKN i.e., $Na_{0.2}K_{0.8}NbO_3$ samples are significantly promoting the osteogenic differentiation as compared to E. S. Neg. $Na_{0.5}K_{0.5}NbO_3$ samples.

3.8.2.3. Morphological analyses. The response of the hMSCs on the non-treated and treated (Electrostatically/dynamically stimulated) piezoelectric $Na_xK_{1-x}NbO_3$ and control samples were qualitatively measured in terms of morphology and projected area of adhered cells, as illustrated in Figs. 12 (a) and (b). It can be seen that the dynamic pulsed electric field treated non-Pol. or polarized NKN samples and the Neg. Pol. NKN samples reveal elongated morphology of adhered hMSCs [Fig. 12 (a)]. In addition, well-organized polygon-shaped and more elongated morphology of adhered cells can be observed on the electrically stimulated Neg. Pol. (E. S. Neg.) NKN samples than their respective non-Pol., polarized (Pos. or Neg. Pol.), E. S. and E. S. Pos. samples. The area measurement analyses of adhered cells further revealed that the treated piezoelectric NKN samples demonstrate significantly higher spreading of adhered hMSCs than the control samples, treated with a similar method [Fig. 12 (b)]. In addition, the Neg. Pol., electrically stimulated, E. S. Neg. and E. S. Pos. NKN samples are revealing a significant increase in the projected area of adhered hMSCs than non-Pol. NKN [Fig. 12 (b)]. Among different treated (Electrostatically/dynamically stimulated) NKN samples, the E. S. Neg. $Na_xK_{1-x}NbO_3$ (x = 0.2, 0.5, 0.8) samples demonstrate the highest area of adhered cells, which is measured to be (262, 250, 270 %) of the mean projected area of hMSCs cells, adhered on non-Pol. HA samples [Fig. 12 (b)].

3.8.2.4. Intracellular Ca^{2+} concentration. The level of intracellular Ca^{2+} on non-treated and treated (Electrostatically/dynamically stimulated) piezoelectric $Na_xK_{1-x}NbO_3$ and control samples, obtained using intracellular Ca^{2+} fluorescence indicator Fura-2 AM loaded MG-63 cells, are illustrated in terms of the mean of the peak values of the ratio of fluorescence intensity at 340 and 380 nm [Fig. 13]. The level of intracellular Ca^{2+} is found to be significantly higher on the non-Pol. and polarized NKN samples, cultured under dynamic pulsed electrical stimulation as compared to the non-Pol. and polarized control HA samples, cultured in the absence or presence of electrical stimulation [Fig. 13]. In addition, all of the Neg. Pol. and dynamic electrically stimulated (E. S., E. S. Pos. and E. S. Neg.) samples are revealing a significant rise in the level of intracellular Ca^{2+} as compared to the corresponding non-Pol. NKN samples [Fig. 13]. The level of intracellular Ca^{2+} on negatively polarized and all of the dynamic pulsed electrical stimulation (Neg. Pol., E. S., E. S. Pos., E. S. Neg.) treated $Na_xK_{1-x}NbO_3$; x = 0.2, x = 0.5 and x = 0.8 samples are measured to be (2.1, 2, 2.2, 2.9 times of non-Pol. HA), (2.1, 2.1, 2, 2.7 times of non-Pol. HA) and (2.3, 2.2, 2.3, 3.1 times of non-Pol. HA), respectively. However, it is comparatively lower (1.5, 1.5, 1.6, and 1.8 times of non-Pol. HA) on HA samples. Interestingly, the dynamic pulsed electrically stimulated Neg. Pol. Na-rich NKN i.e., $Na_{0.8}K_{0.2}NbO_3$ and K-rich NKN i.e., $Na_{0.2}K_{0.8}NbO_3$ samples are showing a comparatively higher increase in the level of intracellular Ca^{2+} than similarly treated $Na_{0.5}K_{0.5}NbO_3$ samples, which is consistent with the cellular response on treated samples [Figs. 9–12]. Overall, the synergistic action of electrostatic-dynamic stimulation increases the concentration of Ca^{2+} in MG-63 cells and thereby, positively regulates the functionality of cells, cultured preferably on dynamic electrically stimulated Neg. Pol. NKN samples.

4. Discussion

Overall, the above results clearly infer that the dynamic pulsed electrical stimulation on the cells, adhered on Neg. Pol. surfaces of Na-rich NKN ($Na_{0.8}K_{0.2}NbO_3$) and K-rich NKN ($Na_{0.2}K_{0.8}NbO_3$) samples revealed augmented cell adhesion, proliferation and differentiation [Figs. 9–12]. The Neg. Pol. surfaces of NKN exhibit significantly higher hydrophilicity as compared to their respective non-Pol. and Pos. Pol. NKN and HA control, in DI water and cell culture media [Fig. 8]. XPS analyses also revealed that the surface polarization facilitates the accumulation of oxygen vacancies which form active sites for water adhesion and thereby, increase the surface hydrophilicity [Fig. 7 (b)] [74,75,76,77]. The enhanced hydrophilicity of the Neg. Pol. surfaces augment cellular response [9,78,80,81]. The Neg. Pol. surfaces attract the positively charged cations (Ca^{2+}, H^+ ions) from the biological fluid which further attract the negatively charged proteins (fibronectin and integrin) and therefore, Neg. Pol. surfaces act as a stimulus for cellular adhesion and proliferation [Fig. 14 (a)] [3,9]. In the present study, the dynamic pulsed electrical stimulation was applied, while the cells are being adhered on the polarized samples, after 12 and 24 h of culture. Previous studies reported that the local electric field in the extracellular matrix activates the voltage-gated Ca^{2+} channels, present on the cellular membrane and changes the configuration of receptor channels in the endoplasmic reticulum [Fig. 14 (b)] [3,37]. Consequently, the local electric field facilitates the influx of Ca^{2+} ions from the extracellular microenvironment and endoplasmic reticulum. The increased concentration of intracellular Ca^{2+} ions activates calcium modulated protein and other relevant factors, responsible for the synthesis of bone morphogenic protein (BMP-2) and transforming growth factor (TGF-β), which helps in regulating cellular metabolism [3,37,82]. Therefore, the dynamic pulsed electrical stimulation and negatively charged polarization synergistically contribute in promoting cellular adhesion, proliferation and differentiation.

Another noticeable key point is that the Na and K-rich compositions of NKN i.e., $Na_{0.8}K_{0.2}NbO_3$ and $Na_{0.2}K_{0.8}NbO_3$ are comparatively more favorable for the attachment and proliferation of MG-63 cells and hMSCs than $Na_{0.5}K_{0.5}NbO_3$ samples. The ion dissolution study using ICP analyses indicates that the concentration of Na^+ and K^+, leached in SBF was comparatively higher for Na and K-rich compositions i.e., $Na_{0.8}K_{0.2}NbO_3$ and $Na_{0.2}K_{0.8}NbO_3$ than $Na_{0.5}K_{0.5}NbO_3$ [Fig. 5]. The leaching of Na^+ or K^+ causes a slight increase in the pH of culture media which may be one of the major reasons for the augmented cellular response on Na and K-rich compositions of NKN [83,84,85]. Overall, the synergistic action of surface polarization charge, dynamic pulsed electrical stimulation and optimized compositional modification provide a novel pathway to improve the biological response of NKN piezobioceramics.

5. Conclusions

In the present study, $Na_xK_{1-x}NbO_3$ (x = 0.2–0.8) samples revealed monoclinic geometry with space group P1m1 which was confirmed by Rietveld refinement analyses. The X-ray peak profile analyses suggested that the Na- ($Na_{0.8}K_{0.2}NbO_3$) and K- ($Na_{0.2}K_{0.8}NbO_3$) rich compositions of NKN are showing comparatively smaller crystallite size than $Na_{0.5}K_{0.5}NbO_3$. The measured Vicker's hardness and compressive strength of $Na_xK_{1-x}NbO_3$ (x = 0.2, 0.5, 0.8) samples are (123, 138, 145 %) and (149, 157, 167 %) of HA. ICP-AES analyses demonstrate comparatively higher leaching of Na^+ and K^+ in SBF, for Na and K-rich compositions of NKN, respectively. The negatively charged surfaces of NKN samples showed considerable improvement in surface hydrophilicity and remarkably promote early-stage cellular adhesion. The electrostatic surface polarization charge and dynamic pulsed electrical stimulation synergistically augment cellular proliferation, adhesion and differentiation, preferably on the Neg. Pol. surface of Na and K-rich compositions of NKN. The remarkable improvement in the cellular activity on the electrostatic-dynamic electric field stimulated NKN samples occurs due to the modulation of the metabolic signaling pathway of cells which was confirmed by the measurement of intracellular Ca^{2+} ions.

CRediT authorship contribution statement

Deepak Khare: Experimentation, Result Analyses, Writing - Original draft preparation.

Priya Singh: Phase Analyses, Software.

Ashutosh Kumar Dubey: Conceptualization, Reviewing and Editing, Supervision.

Declaration of competing interest

The authors declare no conflicts of interest.

Acknowledgments

The financial support from SERB, DST, Govt. of India and CST, UP is gratefully acknowledged.

References

[1] E. Fukada, I. Yasuda, On the piezoelectric effect of bone, J. Phys. Soc. Jpn. 12 (1957) 1158–1162.
[2] F.R. Baxter, C.R. Bowen, I.G. Turner, A.C.E. Dent, Electrically active bioceramics: a review of interfacial responses, Ann. Biomed. Eng. 38 (2010) 2079–2092.
[3] D. Khare, B. Basu, A.K. Dubey, Electrical stimulation and piezoelectric biomaterials for bone tissue engineering applications, Biomaterials 258 (2020), 120280.
[4] T. Kobayashi, S. Nakamura, K. Yamashita, Enhanced osteobonding by negative surface charges of electrically polarized hydroxyapatite, J. Biomed. Mater. Res. 57 (2001) 477–484.
[5] W. Chen, Z. Yu, J. Pang, P. Yu, G. Tan, C. Ning, Fabrication of biocompatible potassium sodium niobate piezoelectric ceramic as an electroactive implant, Materials 10 (2017) 18–21.
[6] M.E. Mycielska, M.B.A. Djamgoz, Cellular mechanisms of direct-current electric field effects: galvanotaxis and metastatic disease, J. Cell Sci. 117 (2004) 1631–1639.
[7] G. Thrivikraman, G. Madras, B. Basu, Intermittent electrical stimuli for guidance of human mesenchymal stem cell lineage commitment towards neural-like cells on electroconductive substrates, Biomaterials 35 (2014) 6219–6235.
[8] G. Thrivikraman, S.K. Boda, B. Basu, Unravelling the mechanistic effects of electric field stimulation towards directing stem cell fate and function: a tissue engineering perspective, Biomaterials 150 (2018) 60–86.
[9] A.K. Dubey, B. Basu, Pulsed electrical stimulation and surface charge induced cell growth on multistage spark plasma sintered hydroxyapatite-barium titanate piezobiocomposite, J. Am. Ceram. Soc. 97 (2014) 481–489.
[10] A.K. Dubey, H. Yamada, K. Kakimoto, Space charge polarization induced augmented in vitro bioactivity of piezoelectric (Na, K) NbO3, J. Appl. Phys. 114 (2013), 124701-124701.
[11] A.K. Dubey, K. Kakimoto, A. Obata, T. Kasuga, Enhanced polarization of hydroxyapatite using the design concept of functionally graded materials with sodium potassium niobate, RSC Adv. 4 (2014) 24601–24611.
[12] A.K. Dubey, R. Kinoshita, K. Kakimoto, Piezoelectric sodium potassium niobate mediated improved polarization and in vitro bioactivity of hydroxyapatite, RSC Adv. 5 (2015) 19638–19646.
[13] B. Tandon, J. Blaker, S. Cartmell, Piezoelectric materials as stimulatory biomedical materials and scaffolds for bone repair, Acta Biomater. 73 (2018) 1–20.
[14] T. Yao, J. Chen, Z. Wang, J. Zhai, Y. Li, J. Xing, S. Hu, G. Tan, S. Qi, Y. Chang, P. Yu, C. Ning, The antibacterial effect of potassium-sodium niobate ceramics based on controlling piezoelectric properties, Colloids Surf. B: Biointerfaces 175 (2019) 463–468.
[15] A. Verma, A. Sharma, A. Kumar, A. Mukhopadhyay, D. Kumar, A. Dubey, Multifunctional response of piezoelectric sodium potassium niobate (NKN) toughened hydroxyapatite based biocomposites, ACS Appl. Biol. Mater. 3 (2020) 5287–5299.
[16] A. Verma, D. Kumar, A. Dubey, Antibacterial and cellular response of piezoelectric Na0.5K0.5NbO3 modified 1393 bioactive glass, Mater. Sci. Eng. C 116 (2020), 111138.
[17] D. Khare, A. Singh, A.K. Dubey, Influence of Na and K contents on the antibacterial response of piezoelectric biocompatible NaxK1-xNbO3 (x = 0.2–0.8), Mater Today Commun. 27 (2021), 102317.
[18] D.W. Seldin, G. Giebisch, The Regulation of Sodium And Chloride Balance, Raven Press, New York, 1990.
[19] P. Strazzullo, C. Leclercq, Sodium, in: Advances in Nutrition 5, 2014, pp. 188–190. Bethesda, Md.
[20] N. Marins, R. Silva, C. Ferrua, D. Łukowiec, A. Barbosa, J. Ribeiro, F. Nedel, E. Zavareze, T. Tański, N. Carreño, Fabrication of electrospun poly(lactic acid) nanoporous membrane loaded with niobium pentoxide nanoparticles as a potential scaffold for biomaterial applications, J. Biomed. Mater. Res.BAppl. Biomater. 108 (2020) 1559–1567.
[21] J. Ge, F. Wang, Z. Xu, X. Shen, C. Gao, D. Wang, G. Hu, J. Gu, T. Tang, J. Wei, Influences of niobium pentoxide on roughness, hydrophilicity, surface energy and protein absorption, and cellular responses to PEEK based composites for orthopedic applications, J. Mater. Chem. B 8 (2020) 2618–2626.
[22] M. Niinomi, Fatigue performance and cyto-toxicity of low rigidity titanium alloy, Ti–29Nb–13Ta–4.6Zr, Biomaterials 24 (2003) 2673–2683.
[23] Y. Zhang, D. Sun, J. Cheng, J. Tsoi, J. Chen, Mechanical and biological properties of Ti–(0–25 wt%)Nb alloys for biomedical implants application, Regen. Biomater. 7 (2020) 119–127.
[24] L. de Souza, J. Lopes, F. Ferreira, R. Martin, C. Bertran, C. Camilli, Evaluation of effectiveness of 45S5 bioglass doped with niobium for repairing critical-sized bone defect in in vitro and in vivo models, J. Biomed. Mater. Res.A 108 (2020) 446–457.
[25] L. Bonetti, L. Altomare, N. Bono, E. Panno, C. Campiglio, L. Draghi, G. Candiani, S. Farè, A. Boccaccini, L. Nardo, Electrophoretic processing of chitosan based composite scaffolds with Nb-doped bioactive glass for bone tissue regeneration, J. Mater. Sci.Mater. Med. 31 (2020).
[26] A. Sobczak, Z. Kowalski, Z. Wzorek, Preparation of hydroxyapatite from animal bones, Acta Bioeng. Biomech. 11 (4) (2009) 23.
[27] V.S. Kattimani, S. Kondaka, K.P. Lingamaneni, Hydroxyapatite—past, present, and future in bone regeneration, Bone Tissue Regen. Insights 7 (2016) 9.
[28] M.H. Santos, M. Oliveira, L.P.F. Souza, H.S. Mansur, W.L. Vasconcelos, Synthesis control and characterization of hydroxyapatite prepared by wet precipitation process, Mater. Res. 7 (2004) 625–630.
[29] ASTM E3484-99 A, Standard Test Method for Micro Indentation Hardness of Materials, 1984.
[30] A. Oyane, H.M. Kim, T. Furuya, T. Kokubo, T. Miyazaki, T. Nakamura, Preparation and assessment of revised simulated body fluids, J. Biomed. Mater. Res. 65A (2003) 188–195.
[31] J. Clover, M. Gowen, Are MG-63 and HOS TE85 human osteosarcoma cell lines representative models of the osteoblastic phenotype? Bone 15 (1994) 585–591.
[32] Y. Su, X. Luo, B.C. He, Y. Wang, L. Chen, G.W. Zuo, B. Liu, Y. Bi, J. Huang, G. H. Zhu, Y. He, Q. Kang, J. Luo, J. Shen, J. Chen, X. Jjin, R.C. Haydon, T.C. He, H. H. Luu, Establishment and characterization of a new highly metastatic human osteosarcoma cell line, Clin. Exp. Metastasis 26 (2009) 599–610.
[33] X.S. Zhan, S.E. Ashram, D.Z. Luo, H.N. Luo, B.Y. Wang, S.F. Chen, Y.S. Bai, Z. S. Chen, C.Y. Liu, H.Q. Ji, A comparative study of biological characteristics and transcriptome profiles of mesenchymal stem cells from different canine tissue, Int. J. Mol. Sci. 20 (2009) 1485.
[34] P.G. Robey, The biochemistry of bone, Endocrinol. Metab. Clin. N. Am. 18 (1989) 859–902.
[35] E.E. Golub, K. Boesze-Battaglia, The role of alkaline phosphatase in mineralization, Curr. Opin. Orthop. 18 (2007) 444–448.
[36] N.S. Fedarko, P. Bianco, U. Vetter, P.G. Gehron, Human bone cell enzyme expression and cellular heterogeneity: correlation of alkaline phosphatase enzyme activity with cell cycle, J. Cell. Physiol. 114 (1990) 115–121.
[37] N. More, G. Kapusetti, Piezoelectric material - a promising approach for bone and cartilage regeneration, Med. Hypoth. 108 (2017) 10–16.
[38] M.D. Bootman, M.J. Berridge, H.L. Roderick, Calcium signalling: more messengers, more channels, more complexity, Curr. Biol. 12 (2002) 563e5.
[39] G. Song, G. Ouyang, S. Bao, The activation of Akt/PKB signaling pathway and cell survival, J. Cell. Mol. Med. 9 (2005) 59e71.
[40] S. Staehlke, A. Koertge, B. Nebe, Intracellular calcium dynamics dependent on defined microtopographical features of titanium, Biomaterials 46 (2015) 48–57.
[41] Y. Shao, M. Alicknavitch, M.C. Farach-Carson, Expression of voltage sensitive calcium channel (VSCC) L-type Cav1.2 (alpha1C) and T-type Cav3.2 (alpha1H) subunits during mouse bone development, Dev. Dyn. 234 (2005) 54e62.
[42] F.D. Virgilio, T.H. Steinberg, S.C. Silverstein, Inhibition of Fura-2 sequestration and secretion with organic anion transport blockers, Cell Calcium 11 (1990) 57–62.
[43] C. Suryanarayana, M.G. Norton, X-ray Diffraction: A Practical Approach, Plenum Press Publishing, New York, 1998.
[44] S. Sarkar, R. Das, Shape effect on the elastic properties of Ag nanocrystals, micro, Nano Lett. 13 (2018) 312–315.
[45] M.A. Tagliente, M. Massaro, Strain-driven (002) preferred orientation of ZnO nanoparticles in implanted silica, Nucl. Instrum. Methods Phys. Res. B. 266 (2008) 1055–1061.
[46] R. Jacob, J. Isac, X-ray diffraction line profile analyses of Ba0.6Sr0.4FexTi1-x O3-δ, Int. J. Chem. Stud. 2 (2015) 12–21.
[47] K.A. Zak, A.W.H. Majid, M.E. Abrishami, R. Yousefi, X-ray analysis of ZnO nanoparticles by Williamson-Hall and size-strain plot methods, Solid State Sci. 13 (2011) 251.
[48] R.D. Shannon, Revised effective ionic radii and systematic studies of interatomic distances in halides and chalcogenides, Acta Cryst. A 32 (1976) 751–767.
[49] J. Tellier, B. Malic, B. Dkhil, D. Jenko, J. Cilensek, M. Kosec, Crystal structure and phase transitions of sodium potassium niobate perovskites, Solid State Sci. 11 (2009) 320–324.
[50] M. Rabiei, A. Palevicius, A. Monshi, S. Nasiri, A. Vilkauskas, G. Janusas, Comparing methods for calculating nano crystal size of natural hydroxyapatite using X-ray diffraction, Nanomaterials 10 (2020) 1627.
[51] D. Hull, D.J. Bacon, Chapter 3 - movement of dislocations, in: D. Hull, D.J. Bacon (Eds.), Introduction to Dislocations, Fifth Edition, Butterworth-Heinemann, 2011, pp. 43–62.
[52] T.O. Erinosho, F.P.E. Dunne, Lattice strain distributions due to elastic distortions and GND development in polycrystals, J. Mech. Phys. Solids 67 (2014) 62–86.
[53] K. Shalini, N.V. Giridharan, Coexistence of electric polarization and magnetic ordering in acceptor doped potassium sodium niobate (KNN) ceramics, Mater. Res. Express 5 (2018), 09610.
[54] D. Nath, F. Singh, R. Das, X-ray diffraction analysis by Williamson-Hall, Halder-Wagner and size-strain plot methods of CdSe nanoparticles- a comparative study, Mater. Chem. Phys. 239 (2020), 122021.
[55] P. Sumit, A. Avinash, K. Rai, Development of high strength hydroxyapatite for hard tissue replacement, Trends Biomater. Artif. Organs 19 (2005) 46–51.
[56] J.Y. Rho, M.E. Roy, T.Y. Tsui, G.M. Pharr, Elastic properties of microstructural components of human bone tissue as measured by nanoindentation, J. Biomed. Mater. Res. 45 (1999) 48–54.
[57] P.K. Zysset, X.E. Guo, C.E. Hoffler, K.E. Moore, S.A. Goldstein, Elastic modulus and hardness of cortical and trabecular bone lamellae measured by nanoindentation in the human femur, J. Biomech. 32 (1999) 1005–1012.
[58] D.T. Reilly, A.H. Burstein, The elastic and ultimate properties of compact bone tissue, J. Biomech. 8 (1975) 393–396.

[59] E.F. Morgan, G.U. Unnikrisnan, A.I. Hussein, Bone mechanical properties in healthy and diseased states, Annu. Rev. Biomed. Eng. 20 (2018) 119–143.
[60] G. Shirane, R. Newnham, R. Pepinsky, Dielectric properties and phase transitions of NaNbO3 and (Na, K)NbO3, Phys. Rev. 96 (1954) 581.
[61] A. Saxena, K. Kakimoto, A.K. Dubey, Polarization induced dielectric and electrical response of electrovector hydroxyapatite and ferroelectric sodium potassium niobate ceramics, J. Phys. D: Appl. Phys. 53 (2020), 395402.
[62] L. Wang, W. Ren, W. Ma, M. Liu, P. Shi, X. Wu, Improved electrical properties for Mn-doped lead-free piezoelectric potassium sodium niobate ceramics, AIP Adv. 5 (2015), 097120.
[63] V.V. Atuchin, I.E. Kalabin, V.G. Kesler, N.V. Pervukhina, Nb 3d and O 1s core levels and chemical bonding in niobates, J. Electron Spectrosc. Relat. Phenom. 142 (2005) 129–134.
[64] R. Shyam, D. Negi, P. Vashishtha, G. Gupta, A. Das, P. Dobbidi, S.R. Nelamarri, Study of light-emitting defects induced by 100 MeV Ag ion irradiation in potassium sodium niobate thin films, J. Lumin. 233 (2021), 117909.
[65] J.F. Moulder, W.F. Stickle, P.E. Sobol, K.D. Bomben, Handbook of X-ray Photoelectron Spectroscopy: A Reference Book of Standard Spectra for Identification And Interpretation of XPS Data 45, Perkin-Elmer Corporation, Waltham, MA, 1992.
[66] M. Wegmann, L. Watson, A. Hendry, XPS analysis of submicrometer barium titanate powder, J. Am. Ceram. Soc. 87 (2004) 371–377.
[67] X. Chen, L. Liu, P.Y. Yu, S.S. Mao, Increasing solar absorption for photocatalysis with black hydrogenated titanium dioxide nanocrystals, Science 331 (2011) 746–750.
[68] Y. Shuai, S. Zhou, D. Bürger, H. Reuther, I. Skorupa, V. John, M. Helm, H. Schmidt, Decisive role of oxygen vacancy in ferroelectric versus ferromagnetic Mn-doped BaTiO3 thin films, J. Appl. Phys. 109 (2011), 084105.
[69] W. Hu, Y. Liu, R.L. Withers, T.J. Frankcombe, L. Norén, A. Snashall, M. Kitchin, P. Smith, B. Gong, H. Chen, J. Schiemer, F. Brink, J. Wong-Leung, Electron-pinned defect-dipoles for high-performance colossal permittivity materials, Nat. Mater. 12 (2013) 821–826.
[70] J. Hu, L. Wang, L. Shi, H. Huang, Preparation of La1−xCaxMnO3 perovskite–graphene composites as oxygen reduction reaction electrocatalyst in alkaline medium, J. Power Sources 269 (2014) 144–151.
[71] C.C. Lin, C.C. Chen, C.M. Weng, S.Y. Chu, C.S. Hong, C.-C. Tsai, Effects of lithium doping on microstructure, electrical properties, and chemical bonds of sol-gel derived NKN thin films, J. Appl. Phys. 117 (2015), 085307.
[72] E.R. Moore, P. Ferrari, D.E. Diaz-Droguett, D. Lederman, J.T. Evans, Raman and X-ray photoelectron spectroscopy study of ferroelectric switching in Pb(Nb, Zr, Ti)O3 thin films, J. Appl. Phys. 111 (2012) 14108.
[73] X. Li, Y. Wang, W. Liu, G. Jiang, C. Zhu, Study of oxygen vacancies' influence on the lattice parameter in ZnO thin film, Mater. Lett. 85 (2012) 25–28.
[74] L. Wan, W. Tian, N. Li, D. Chen, Q. Xu, H. Li, J. He, J. Lu, Hydrophilic porous PVDF membrane embedded with BaTiO3 featuring controlled oxygen vacancies for piezocatalytic water cleaning, Nano Energy 94 (2022), 106930.
[75] R. Schaub, P. Thostrup, N. Lopez, E. Lægsgaard, I. Stensgaard, J.K. Nørskov, F. Besenbacher, Oxygen vacancies as active sites for water dissociation on rutile TiO2 (110), Phys. Rev. Lett. 87 (2001), 266104.
[76] H. Hu, H.F. Ji, Y. Sun, The effect of oxygen vacancies on water wettability of a ZnO surface, Phys. Chem. Chem. Phys. 15 (2013) 16557–16565.
[77] H. Yu, J. Li, Y. Zhang, S. Yang, K. Han, F. Dong, T. Ma, H. Huang, Three-in-one oxygen vacancies: whole visible-spectrum absorption, efficient charge separation, and surface site activation for robust CO2 photoreduction, Angew. Chem. Int. Ed. 58 (2019) 3880–3884.
[78] K. Das, S. Bose, A. Bandyopadhyay, Surface modifications and cell-materials interactions with anodized Ti, Acta Biomater. 3 (2007) 573–585.
[79] N. Yamada, T. Okano, H. Sakai, F. Karikusa, Y. Sawasaki, Y. Sakurai, Thermoresponsive polymeric surfaces – control of attachment and detachment of cultured-cells, Makromol. Chem.RapidCommun. 11 (1990) 571–576.
[80] B.A. Dikici, S. Dikici, O. Karaman, H. Oflaz, The effect of zinc oxide doping on mechanical and biological properties of 3D printed calcium sulfate based scaffolds, Biocyber.Biomed. Eng. 37 (2017) 733–741.
[81] K. Webb, V. Hlady, P.A. Tresco, Relative importance of surface wettability and charged functional groups on NIH 3T3 fibroblast attachment, spreading, and cytoskeletal organization, J. Biomed. Mater. Res. 41 (1998) 422–430.
[82] J. Jacob, N. More, K. Kalia, G. Kapusetti, Piezoelectric smart biomaterials for bone and cartilage tissue engineering, Inflamm. Regen. 38 (2018).
[83] M. Uo, M. Mizuno, Y. Kuboki, A. Makishima, F. Watari, Properties and cytotoxicity of water soluble Na2O–CaO–P2O5 glasses, Biomaterials 19 (1998) 2277–2284.
[84] T. Arnett, Extracellular pH regulates bone cell function, J. Nutr. 138 (2008) 415S–418S.
[85] A. Galow, A. Rebl, D. Koczan, S. Bonk, W. Baumann, J. Gimsa, Increased osteoblast viability at alkaline pH in vitro provides a new perspective on bone regeneration, Biochem. Biophys. Rep. 10 (2017) 17–25.